Sub-cloud rain evaporation in the North Atlantic winter trades derived by pairing isotopic data with a bin-resolved microphysical model

Mampi Sarkar[1], Adriana Bailey[1], Peter Blossey[2], Simon P. de Szoeke[3], David Noone[4], Estefania Quinones Melendez[3], Mason D. Leandro[5], and Patrick Y. Chuang[5]

[1]National Center for Atmospheric Research, Boulder, Colorado, USA
[2]University of Washington, Washington, USA
[3]Oregon State University, Oregon, USA
[4]University of Auckland, New Zealand
[5]University of California, Santa Cruz, California, USA

Correspondence: Mampi Sarkar (msarkar2@uh.edu)

Abstract. Sub-cloud rain evaporation in the trade wind region significantly influences boundary layer mass and energy budgets. Parameterizing it is, however, difficult due to the sparsity of well-resolved rain observations and the challenges of sampling short-lived marine cumulus clouds. In this study, sub-cloud rain evaporation is analyzed using a steady-state one-dimensional model that simulates changes in drop sizes, relative humidity, and rain isotopic composition. The model is initialized with relative humidity, raindrop size distributions, and water vapor isotope ratios (e.g. δD_v, $\delta^{18}O_v$) sampled by the NOAA P3 aircraft during the Atlantic Tradewind Ocean-Atmosphere Mesoscale Interaction Campaign (ATOMIC), which was part of the larger EUREC[4]A (ElUcidating the RolE of Clouds-Circulation Coupling in ClimAte) field program. The modeled surface precipitation isotope ratios closely match observations from EUREC[4]A ground-based and ship-based platforms, lending credibility to our model. The model suggests that 63% of the rain mass evaporates in the sub-cloud layer across 22 P3 cases. The vertical distribution of the evaporated rain flux is 'top-heavy' for a narrow (σ) raindrop size distribution (RSD) centered over a small geometric mean diameter (D_g) at the cloud base. A 'top-heavy' profile has higher rain evaporated fraction (REF) and larger changes in rain deuterium excess ($d=\delta D$-8$\times\delta^{18}O$) between the cloud base and the surface, than a 'bottom-heavy' profile which results from a wider RSD with larger D_g. The modeled REF and change in d are also more strongly influenced by cloud base D_g and σ rather than the concentration of raindrops. The model results are accurate so long as variations in relative humidity conditions are accounted for. Relative humidity alone, however, is a poor indicator of sub-cloud rain evaporation. Overall, our analysis indicates the intrinsic dependence of sub-cloud rain evaporation on both thermodynamic and microphysical processes in the trade wind region.

1 Introduction

Shallow precipitation is a sporadic but energetically significant feature of marine cumulus clouds in the trade-wind tropical ocean basins (Byers and Hall, 1955; Nicholls and Leighton, 1986; Paluch and Lenschow, 1991; Short and Nakamura, 2000;

Jensen et al., 2000; Stevens, 2005). Rain rates on the scale of 1 mm/day, commonly associated with shallow cumulus precipitation, are capable of producing roughly 28 Wm^{-2} of latent heat flux through rain evaporation in the sub-cloud layer (Figure 1), which is comparable to the radiative and surface fluxes computed using mixed layer models (e.g. Caldwell et al., 2005) and within stratocumulus-to-cumulus transition regions (e.g. Kalmus et al., 2014).

Such large fluxes, even if localized, may influence the vertical moisture and energy distribution and affect the boundary layer stability (e.g. Srivastava, 1985; Paluch and Lenschow, 1991). The evaporatively cooled air mass also facilitates downdrafts below the cloud base which initiate or strengthen cold pool formations (Srivastava, 1985; Jensen et al., 2000; Seifert, 2008; Zuidema et al., 2012; de Szoeke et al., 2017). The downdraft can further feed its cool and moist air into large-scale circulations leading to moisture recycling (Stevens, 2005; Worden et al., 2007). A schematic of these processes is shown in Figure 1.

The rain evaporation efficiency, or the fraction of rain evaporated in the sub-cloud layer, impacts the amount of rain that reaches the surface. Depending on the fraction of rain reaching the surface and the sub-cloud moisture circulations, clouds could either remain intact or break up affecting the local albedo (Paluch and Lenschow, 1991; Sandu and Stevens, 2011; Yamaguchi et al., 2017; O et al., 2018; Sarkar et al., 2020). Overall, accurate rain evaporation estimates in shallow cumulus regions are needed to better predict surface rain estimates in weather and climate models, and understand the shallow rain life cycle.

Past field campaigns have sampled precipitation from shallow cloud systems. For example, the Atlantic Stratocumulus Transition Experiment (ASTEX, Bretherton and Pincus, 1995) conducted over the east-central Atlantic Ocean in June 1992, sampled with drizzle evaporating into the sub-cloud layer beneath overlying stratocumulus clouds. Similarly, the Rain in Cumulus over the Ocean (RICO, Geoffroy et al., 2014; Snodgrass et al., 2009) campaign was conducted off the Caribbean islands of Antigua and Barbuda over the Atlantic Ocean in 2012-2013, where cumulus rain was sampled. Further, the Cloud System Evolution in the Trades (CSET, Albrecht et al., 2019; Mohrmann et al., 2019; Sarkar et al., 2020) was conducted over the Pacific Ocean between California and Hawaii in July-August 2015 to sample stratocumulus and cumulus rain events. These campaigns support the idea that shallow precipitation and sub-cloud evaporation is important for the local energy budget. However, a more dedicated study is needed to characterize the shallow cloud rain evaporation as a function of the local thermodynamic and microphysical conditions.

Questions also remain about the rain evaporation flux (F_e) variability in different cloud conditions and its sensitivity to boundary layer microphysical and thermodynamic characteristics. How is the vertical structure of F_e linked to microphysical and thermodynamic processes? Could F_e reinforce or weaken sub-cloud stability at local scales? These questions are inherent to our understanding of shallow rain processes and constraining F_e accurately.

A major challenge in observationally constraining rain evaporation is sampling rain in and below cumulus clouds, due mainly to their temporal and spatial variability and the limitations in existing rain retrieval methods. The airborne mm-wavelength radar used during field campaigns provides a wide and homogeneous array of cloud and precipitation samples in terms of radar moments. However, accurate microphysical retrievals from the radar moments are difficult due to Mie scattering and atmospheric and liquid attenuations (Fairall et al., 2018; Schwartz et al., 2019; Sarkar et al., 2021). Rain observations from

satellites, although they provide a large array of datasets, are often limited in their accuracy of sensing shallow rain. This is due to factors like high atmospheric attenuation and surface radar reflections (e.g. Kalmus et al., 2014).

In comparison, in-situ cloud and rain probes, although limited in their sampling volume compared to radar, provide well-resolved, direct, and accurate microphysical raindrop size distributions (RSD). In-situ measurements also provide stable isotope ratios of hydrogen and oxygen in water vapor, which can be used to independently assess rain evaporation. This is because as rain evaporates into the unsaturated sub-cloud layer, the isotopically light water transitions to the vapor phase more efficiently, causing the drops to become increasingly heavy (Salamalikis et al., 2016; Graf et al., 2019).

This study makes a novel attempt to characterize rain evaporation, its vertical structure, and its dependence on microphysical (i.e. raindrop concentration, size, and distribution width) and thermodynamic (i.e. surface relative humidity) features using a one-dimensional steady-state evaporation model initialized by in-situ field observations of both RSD and water vapor isotope ratios. The in-situ samples were measured by the NOAA WP-3D Orion (P3) aircraft during the Atlantic Tradewind Ocean-Atmosphere Mesoscale Interaction Campaign (ATOMIC), which was a component of the international field campaign known as EUREC^{4}A (ElUcidating the RolE of Clouds-Circulation Coupling in ClimAte). For the first time, the isotopic enrichment of rain is modeled using RSDs measured in the field and evaluated using surface-based isotopic rain observations.

First, the rain observations are characterized at the cloud base in terms of microphysical and thermodynamic conditions. Second, the vertical distribution of the sub-cloud modeled rain water content (RWC) and rain evaporation fluxes (F_e) are discussed in terms of their microphysical and thermodynamic sensitivities. Last, the modeled isotope ratios at the surface are also compared with the surface isotope ratio observations in the P3 vicinity, to validate the accuracy of the model. We expect results from this work to pave the way toward a better representation of shallow rain evaporation in climate models and to serve as a model for comparing rain evaporation processes in a wide range of convection.

2   Data and Methodology

2.1   ATOMIC/EUREC^{4}A campaign and datasets

The ATOMIC field campaign was conducted in the North Atlantic trade wind region roughly, between 51°W-60°W and 10°N-15°N to study mesoscale circulations in the atmosphere and ocean (Pincus et al. 2021). ATOMIC was the NOAA-sponsored component of the larger, international EUREC^{4}A field campaign which took place in January-February 2020 near Barbados (Stevens et al., 2021). Both the NOAA P3 aircraft and the NOAA R/V Ronald H. Brown (Ron Brown) were deployed as part of ATOMIC. Other platforms, such as the R/V Meteor and Barbados Cloud Observatory (BCO) discussed in this paper, were part of the larger EUREC^{4}A effort.

The P3, integrated with radar, in-situ instruments, and dropsondes, was flown through cloud and rain transects to collect thermodynamic and microphysical boundary layer observations and facilitate investigations of aerosol-cloud-precipitation interactions. An example of the trajectory of the P3 is shown in Figure 2 for 9 February, where a series of stacked 10-minute horizontal legs were flown to sample the boundary layer extensively. The horizontal legs were flown at 150 m, 500 m, 700 m, 2 km, and 3 km between 54°W-56°W. During most flights, a level circle was also conducted at 7.5 km altitude and 7-8 dropson-

des were released to obtain high-resolution thermodynamic observations reaching the surface. The surface relative humidity, which is integral to the rain evaporation model used in this paper, is obtained at ≈10 m altitude. Its values for 9 February are noted at the dropsonde locations in Figure 2b.

This paper characterizes rain structure during ATOMIC using the Cloud Imaging Probe (CIP) and Precipitation Imaging Probe (PIP) instruments on board the P3, which sampled raindrop size distributions in situ. The CIP samples cloud- and rain-drops across diameters of 25 μm-1.6 mm, while the PIP samples across 100μm- 6.2 mm (Pincus et al., 2021; Leandro and Chuang, 2021). The CIP and PIP observations are stitched together to obtain 1-Hz raindrop size distributions for diameters spanning 100 μm-6 mm (total 23 bins). Bin sizes smaller than 100 μm and bigger than 6 mm are not reliable and are not used in the current analysis. Drops across 400-1800 μm, 1.8-5 mm, and 5-6 mm drop sizes are binned at 200 μm, 400 μm, and 1 mm resolutions, respectively.

This paper is based on the later part of the ATOMIC campaign when the CIP and PIP instruments were properly functioning and mean rain rates greater than 0.01 mm/day were observed during 22 10-minute in-cloud horizontal legs on 4, 5, 9, and 10 February. The in-cloud RSD is assumed to accurately represent cloud base RSD. The rain rates (in mm/day) are calculated from the observed RSD using $R = 6\pi \times 10^{-7} \sum_{i=1}^{23} N(D_i) v_i D_i^3$, where N (m^{-3}) is the raindrop concentration for drop diameter D_i (mm), v_i (m/s) is the terminal velocity associated with D_i, and i is the index of the RSD bin. The rain rates for each 10-minute leg are averaged and noted in the legend of Figure 3. Even though the probe instruments were working on 31 January and 11 February, the mean rain rates from those days were below 0.01 mm/day during all of the 10-minute in-cloud horizontal legs and are therefore not included in this study.

To model the isotopic evolution of the RSDs, 1-Hz water vapor mixing ratio and water vapor isotope ratios for hydrogen and oxygen (δD_v and $\delta^{18}O_v$ respectively) were obtained from the Picarro L2130-i water vapor isotope analyzer flown during ATOMIC (Bailey et al., 2023). When airborne, the analyzer drew in ambient air through a 0.25-inch backward-facing tube, which ensured the selective sampling of water vapor as opposed to liquid water (Pincus et al., 2021). δD_v and $\delta^{18}O_v$ represent the ratios D/H and $^{18}O/^{16}O$, respectively, normalized to VSMOW (Vienna Standard Ocean Water) and reported in units permil (‰). The standard deviations associated with the 1-Hz P3 δD_v and $\delta^{18}O_v$ for specific humidity of 1-18 g/kg are 2 ‰ and 0.8‰, respectively (Figure 8, Bailey et al. (2023)).

The accuracy of the sub-cloud rain evaporation model used in this study is evaluated using the rain isotope ratios and rain rate measurements from the NOAA Research Vessel Ronald H. Brown (ship). During ATOMIC, the Brown sailed in the trade-wind region between Barbados and the Northwest Tropical Atlantic Station (NTAS), a buoy station near 15°N, 51°W, to provide a ground-based perspective for the P3 flying overhead. The isotopic composition of 12 precipitation samples collected aboard the Brown has been characterized with 0.2 ‰ and 0.8 ‰ of uncertainty in δD_v and $\delta^{18}O_v$, respectively (Bailey et al., 2023). While the Brown measurements (collected across a wide geographic area between 5 January and 11 February) are not exactly co-located in space or time with the P3, they still provide a useful assessment of the trade-cumulus environment in which the P3 flew.

Isotope ratios were also sampled in surface precipitation at two other stations, viz. the Barbados Cloud Observatory (BCO) and the German R/V Meteor (ship), that were part of the EUREC^{4}A campaign. These provide further observational constraints

for the rain evaporation model used in this study. The BCO is a land-based observatory on the eastern shores of Barbados, where 42 precipitation samples were collected from 16 January and 18 February (Villiger et al., 2021). The Meteor sailed along a north-south transect defined by the 57.24°W meridian and sampled 15 rain events between 20 January and 19 February. Uncertainties associated with the Meteor samples are 0.2‰ and 0.5‰ for $\delta^{18}O_p$ and δD_p, respectively (Galewsky and Los, 2020). More details regarding isotopic observations, stations, and measurement techniques during EUREC4A are described in Bailey et al. (2023).

2.2 Sub-cloud rain evaporation model

Observed raindrop size distributions are used to initialize the sub-cloud rain evaporation model using aircraft data from flights on 4, 5, 9, and 10 February. This one-dimensional steady-state model is used mainly to (a) estimate the amount and vertical distribution of water vapor and the equivalent latent flux produced by the evaporation of raindrops of 125 μm-6 mm diameters, and (b) estimate the change in precipitation isotope ratios δD_p and $\delta^{18}O_p$ of the raindrops during evaporation. The model follows the numerical isotope-evaporation model described in detail in Pruppacher et al. (2010), Graf et al. (2019) and Salamalikis et al. (2016) and predicts vertical variations in the size, temperature and isotopic composition (δD_p and $\delta^{18}O_p$) of raindrops.

The cloud base in the model is deduced from ceilometer observations aboard the Brown. The 10-minute resolved ceilometer observations (Quinn et al., 2021) show that the median cloud bases on 4, 9, and 10 February are between 700-800 m. Consequently, the raindrops are initiated from a 700 m cloud base and modeled to fall through a sub-saturated sub-cloud layer. The relative humidity at the cloud base is assumed to be 100%, decreasing linearly towards the surface (verified from the dropsonde observations, Figure A2) with surface relative humidity varying from 65%-80%, as determined from nearby dropsonde observations. The sub-cloud layer is well-mixed with an average specific humidity from dropsondes varying within 13-15 g/kg across the sub-cloud layer (Figure A2). The rain water content (RWC) is computed at cloud base using the stitched CIP/PIP-based raindrop size distribution.

The model is integrated downward from the initial condition at the cloud base. A nominal step size (Δz) of 1 m is used, but an adaptive step size is employed to ensure the stability of the explicit time integration method. The adaptive time stepping is active for droplets smaller than about 1 mm. Following Graf et al. (2019), the raindrop diameter evolves according to:

$$\frac{dD}{dz} = \frac{4(F_v D_{va})}{D v \rho_w R_v} \left[RH \frac{e_{v,sat}}{T_a} - \frac{e_{r,sat}}{T_r} \right] \tag{1}$$

where,

F_v (unitless): mass ventilation coefficient,

D_{va} (m^{2}s^{-1}): diffusivity of water vapor in air,

R_v (461.5 Jkg^{-1}K^{-1}): gas constant for water vapor,

RH (%): relative humidity,

$e_{v,sat}$, $e_{r,sat}$ (Pa): saturation vapor pressure at ambient temperature and drop surface,

T_a (K): ambient temperature,

T_r (K): raindrop surface temperature,

D (m): raindrop bin diameter,

v (m/s): raindrop terminal velocity,

ρ_w (10^3 kg/m^3): density of water,

z (m): altitude.

The vertical variation of T_r is given by (Graf et al. (2019)):

$$\frac{dT_r}{dz} = \frac{12 F_h k_a}{D^2 \rho_w c_w v}\left(\left(RH\frac{e_{v,sat}}{T_a} - \frac{e_{r,sat}}{T_r}\right)\left(\frac{F_v D_{va} L}{F_h k_a R_v}\right) - (T_r - T_a)\right) \tag{2}$$

where

F_h (unitless): heat ventilation coefficient,

k_a (Jm^{-1}s^{-1}K^{-1}): thermal conductivity of air,

c_w (4187 Jg^{-1}K^{-1}): specific heat of water, and

L (2.25×10^3 J/g): latent heat of vaporization.

While each raindrop size bin (indexed by i) has its own diameter (D_i), temperature ($T_{r,i}$), fall speed (v_i), and vapor pressure ($e_{r,sat,i}$), the subscripts showing the bin index (i) have been dropped in the Equations above for clarity. Note also that size of raindrops in each bin $D_i(z)$ varies with height and the number of droplets in that bin $N(D_i)$, remains fixed for all heights until the droplets evaporate, which is assumed to occur when $D_i(z) < 1\mu$m.

The calculated D at vertical level z is then used to model the steady-state RWC (gm^{-3}) at z using:

$$RWC = \frac{\pi}{6}\rho_w \sum_{i=1}^{23} N(D_i) D_i^3. \tag{3}$$

The precipitation flux $F_p(z)$ (Wm^{-2}) at each level z for bin index i is modeled using:

$$F_p(z) = \frac{\pi}{6}\rho_w L \sum_{i=1}^{23} v_i N(D_i) D_i^3. \tag{4}$$

The rain evaporation flux produced as the Δz m^3 box falls through Δz depth is given by $F_e(z)$ (Wm^{-2}m^{-1}) at level z using:

$$F_e(z) = -\frac{\partial F_p(z)}{\partial z} = \frac{F_p(z) - F_p(z - \Delta z)}{\Delta z}. \tag{5}$$

The total rain evaporation flux produced over the entire sub-cloud layer F_{eT} (Wm^{-2}) is obtained from:

$$F_{eT} = \int_{sf}^{700m} \frac{\partial F_p(z)}{\partial z}\, dz = \int_{sf}^{700m} F_e(z)\, dz = F_{p,cb} - F_{p,sf}. \tag{6}$$

Rain evaporated fraction (REF) is the fraction of rain evaporated in the sub-cloud layer and is computed based on F_{eT} and $F_{p,cb}$ by:

$$REF = \frac{F_{eT}}{F_{p,cb}} \tag{7}$$

To model the isotopic composition of the precipitation, the vertical change in δ_p (‰) of raindrops as they evaporate is given by (Graf (2017)),

$$\frac{d\delta_p}{dz} = \frac{12e_{r,sat}F_v D_{va}}{\rho_w R_v D^2 T_r v} \times [(\frac{D'_{va}}{D_{va}})^n((\delta_{va}+10^3)RH\frac{e_{v,sat}T_r}{e_{r,sat}T_a} - (\frac{(\delta_p+10^3)}{\alpha_{p\to v}})) - (\delta_p+10^3)(RH\frac{e_{v,sat}T_r}{e_{r,sat}T_a} - 1)]$$ (8)

where δ_p applies to both δD_p and $\delta^{18}O_p$, n=0.58, and D'_{va} is the diffusivity of HDO or $H_2^{18}O$ in air. Equation 8 includes the influences of both evaporation of raindrops and the exchange of isotopes between raindrops and ambient vapor during equilibration. δ_{va} is the mean ambient water vapor isotope ratio expressed in permil (‰), obtained from isotope ratio observations at 150 m altitude. All the parameters discussed in the model are derived from Pruppacher et al. (2010), Graf (2017) and Salamalikis et al. (2016) and are described in the MATLAB code attached.

The rain isotope ratios used to initialize δ_p are determined using in-situ water vapor isotope ratios and the measured temperature at cloud base by assuming that the raindrops are in equilibrium with the water vapor (Risi et al., 2020) and scaling by a temperature-dependent equilibrium fractionation factor ($\alpha_{p->v}$ =(δ_p/1000 +1) /(δ_v/1000 +1)), as defined in Majoube (1971). The modeled δ_p at the surface is later compared with the surface rain isotope ratio observations from the BCO, the Brown, and the Meteor to validate the accuracy of the model.

Because isotope ratios are typically measured in bulk precipitation, we evaluate the mass-weighted isotopic composition of the integrated raindrop size distribution in the simulations. This is done by integrating δD_p and $\delta^{18}O_p$ over the observed RSD to estimate the mean (mass-weighted) δD_p and $\delta^{18}O_p$ at each vertical level z following:

$$\delta_p(z) = \frac{\sum_{i=1}^{23} N(D_i)D_i^3 \delta_{p,i}}{\sum_{i=1}^{23} N(D_i)D_i^3}$$ (9)

The deuterium-excess or d_p, a quantity useful in sub-cloud rain evaporation analysis, is defined as $d_p = \delta D_p - \delta^{18}O_p$. δD_p and $\delta^{18}O_p$ are affected by both equilibrium and non-equilibrium processes in the sub-cloud layer. However, d_p cancels out the equilibrium effects in δD_p and $\delta^{18}O_p$ and thereby only represents the non-equilibrium effects that take place due to rain evaporation in the unsaturated sub-cloud layer.

2.3 Moisture concentration post rain evaporation

Finally, the bulk change in sub-cloud layer absolute humidity resulting from rain evaporation Δq_v (gm^{-3}) can be estimated by assuming an appropriate integration time t (s):

$$\Delta q_v = \int \frac{F_e}{L} dt$$ (10)

.

When the rain-evaporated water vapor mixes with the ambient water vapor then the net isotope ratio at a vertical level z is a combination of the background vapor isotope ratio and the isotope ratio evaporated from the drop as given by Noone (2012):

$$\delta_v = \frac{\delta_e \Delta q_v + \delta_{va} q_{va}}{\Delta q_v + q_{va}}$$ (11)

where δ_e, δ_{va} and δ_v are the isotope ratios (‰) of the evaporated rainwater, ambient water vapor prior to rain evaporation, and total water vapor post rain evaporation at level z, respectively. Δq_v is the result from Equation 10 and depends on both the length of time over which rain evaporation is presumed to occur and on the assumption that the fluxes derived from the steady-state rain evaporation model are constant over the integration interval.

215    $\delta_e(z)$ is computed from the difference between the product of δ_p and RWC at every Δz depth using:

$$\delta_e(z) = \frac{\delta_p(z)RWC(z) - \delta_p(z-\Delta z)RWC(z-\Delta z)}{RWC(z) - RWC(z-\Delta z)} \tag{12}$$

2.4 Microphysical parameters using lognormal fitting

The role of microphysical processes in influencing modeled rain evaporation and rain isotopic composition is investigated in terms of the total raindrop concentration (N_0), geometrical mean diameter (D_g), and the lognormal distribution width (σ) at

220   the sampling level. These parameters (N_0, D_g, and σ) provide physically meaningful quantities to interpret microphysical conditions of rain and are helpful in evaluating the sensitivity of rain evaporation to microphysical changes. These are derived by fitting the observed RSDs to a lognormal distribution (Feingold and Levin (1986)) following:

$$N(D) = N_0 \sum_{i=1}^{23} \frac{1}{D_i\sqrt{2\pi ln^2\sigma}}exp(\frac{-(lnD_i - \mu)^2}{2ln^2\sigma}) \tag{13}$$

where μ is the log of D_g (i.e. $D_g = e^\mu$). $N(D)$ substituted into Equation 4 gives:

225    $$F_p = N_0 \sum_{i=1}^{23} \frac{\pi}{6}\rho_w L \frac{1}{\sqrt{2\pi ln^2\sigma}}exp(\frac{-(lnD_i - \mu)^2}{2ln^2\sigma})D_i^2 v_i. \tag{14}$$

Notice that when $N(D)$ is substituted into Equation 9 for δ_p, N_0 cancels in the numerator and denominator making δ_p (δD_p and $\delta^{18}O_p$) independent of raindrop concentration and only dependent on D_g and σ. Similarly, REF is also almost independent of N_0.

For simplicity, collision-coalescence (i.e., raindrop self-collection) and breakup processes are ignored, as is the impact of

230   turbulence and mesoscale variability. We have assumed that the N_0, D_g, and σ sampled at the in-cloud legs represent the cloud base precipitation well. This assumption is backed by the small difference between the observed N_0, D_g, and σ for a given rain rate whether it is sampled at cloud base or higher (Figure 5). This result is similar to Wood (2005) whose result suggests that the rain rate is near constant in the lower 60% of stratocumulus clouds.

3   Results

235   ### 3.1   Observed rain characteristics

The 10-minute (1-Hz) horizontal leg mean rain rates sampled for 20 out of the 22 cases on 4, 5, 9, and 10 February (Figure 3) vary between 0.01-3 mm/day with rain frequency between 1-10%. The other two cases have more intense rain rates of

22 mm/day and 31 mm/day and rain frequencies of 10% and 50%, respectively, sampled on 9 February at 1630 m and 2112 m altitudes. The leg-mean rain rates are calculated using the 1-Hz samples with rain rates higher than 0.01 mm/day. Rain frequency is defined as the ratio of the number of raining samples to the total number of raining and non-raining samples within a 10-minute horizontal leg. Overall, barring two cases, the rain rates sampled over 20 horizontal legs by the P3 are weak, and comparable with rain usually witnessed in stratocumulus clouds.

The highest and lowest rain rates were observed on 9 February (31 mm/day) and 4 February (0.01 mm/day), respectively. The low rain rates on 4 February are due to the higher concentration of small raindrop diameters (<200 μm) and almost no raindrops larger than 500μm, as compared to the other days. Similarly, the higher rain rates for the two cases on 9 February are due to the high concentrations of larger drops compared to other cases. Seven out of the 22 cases were sampled within ±100 m of cloud base (700 m) while the other cases had sampling altitudes higher than 1.3 km. No rain was detected at any of the 150-m altitude legs (except in one case on 9 February), suggesting that rain either evaporated completely before reaching the surface or was not sampled when it reached the surface.

Vertical and horizontal variability in rain structure is evident in the radar images (Figure 4), which reveal heterogeneous cloud bases and some heavy precipitation pockets with radar reflectivity higher than +10 dBZ. These heavier precipitating samples partially evaporate before reaching the surface. The more weakly precipitating segments, with smaller radar reflectivities, evaporate completely within the sub-cloud layer. Vertical changes in rain structure are also evident from in-situ observed RSDs measured at different altitudes within the same cloud system. For example, on 9 February the RSDs shift towards smaller drop sizes as sampling altitudes decrease from 2112 m to 1630 m to 1500 m to 1053 m (Figure 3c), which could be due to both microphysical and thermodynamic processes in the cloud layer.

3.2 Observed microphysical and thermodynamic variability, compared with CSET and RICO

A strong positive correlation is observed between the rain rates and microphysical parameters N_0, D_g, and σ at cloud base (Figure 5a-c). The higher D_g and σ indicate a higher concentration of larger drops, which account for more liquid water and higher rain rates. While D_g and σ vary modestly (σ by approximately a factor of two), N_0 varies by several orders of magnitude over the 22 P3 cases with rain rates between 0.01-35 mm/day. The 1-Hz distributions of N_0, D_g, σ, and rain rates are plotted in Figure 6 to give an overall microphysical statistical characterization for all the P3 cases. The variability in the rain parameters is the lowest on 4 February and highest on 9 February. The P3 cases also show a weak negative correlation between surface relative humidity (RH$_{sf}$) and rain rate (Figure 5d). This may be due to the downdrafts drying the surface layer and lowering RH$_{sf}$. Note that the correlation of RH$_{sf}$ and rain rate compared to the microphysical variables is weaker as indicated by the r values.

3.2.1 CSET comparison

Compared to the average P3 cases, the cumulus rain events sampled over 5 cases during the CSET campaign in the Northeast Pacific Ocean have higher rain rates (1-100 mm/day) along with higher N_0 (10^3-2×10^4m^{-3}) and σ (2.3) (Figure 5a). However,

the average D_g for the CSET cases lies within the P3 ranges (Figure 5b-c). Since D_g and σ did not vary significantly across the five CSET cases, the higher rain rates during CSET could be due mainly to their larger N_0.

4 out of 5 cases during CSET have RH_{sf} of 84% which is higher than for most of the P3 cases. The correlation between RH_{sf} and rain rate during CSET is much weaker compared to the P3 cases (Figure 5d). RH_{sf} for CSET remains constant at 84% for rain rates from 1 mm/day to 100 mm/day. That said, it is worth noting that RH_{sf} measurements during CSET were collected using aircraft observations at 150 m altitude and, therefore, might differ slightly from the actual surface relative humidity.

The F_{eT} during CSET within some heavily precipitating cumulus transects are between 10-200 Wm^{-2}, comparable to the P3 F_{eT} range of 1-350 Wm^{-2}. The high variability in F_{eT} for both the P3 and CSET events suggests that the heterogeneity of the cumulus rain processes is a common feature across different ocean basins.

3.2.2 RICO comparison

During the RICO campaign, which was based in the Carribbean like the ATOMIC/EUREC4A field campaigns, rain rates sampled were stronger than the P3 cases, as in CSET. The cloud base rain rate is 5 mm/hr during RICO (Figure 2, Geoffroy et al. (2014)). Comparing Figure 6 with Figure 2 in Geoffroy et al. (2014), the median rain rates, N_0, and raindrop diameters during RICO at cloud base were much higher than the P3 cases sampled during ATOMIC. Geoffroy et al. (2014) have used mean volume diameter D_v to describe the variability of their raindrop sizes, which is mathematically different but still comparable to D_g that we have used in this study. D_v at 500 m during RICO is 750 μm which is much higher than D_g of 200 μm during the P3 cases. Similarly, the median N_0 and rain rates during RICO are $6 \times 10^4 m^{-3}$ and 12 mm/hr at 500 m altitude compared to $2 \times 10^3 m^{-3}$ and 3 mm/day, respectively, averages over all the 22 P3 cases. This suggests that the higher rain rates sampled by RICO could have been due to the high N_0 and D_v compared to that sampled by the P3.

All flights during RICO were designed to randomly sample clouds above the cloud base (except one on 19 January), and, as a result, most flights did not sample any precipitation. But the precipitation samples on 19 January suggest a 6% reduction of cloud base rain rate (3 mm/hr) due to rain evaporation (Snodgrass et al., 2009). This roughly translates to 130 Wm^{-2} of rain evaporation flux (based on Figure 10 in Snodgrass et al. (2009)) and is comparable to the CSET and the P3 values.

3.3 Modeled rain evaporation in the sub-cloud layer

3.3.1 Vertical distributions of RWC and F_e

The sub-cloud variability in the rain evaporation over the 22 cases from ATOMIC/EUREC^{4}A is reflected in the vertical profiles of the modeled RWC, rain rate, and F_e in Figure 7d-f. Cases on 9 February, with their highest rain rates and RWC at the cloud base also have the highest RWC reaching the surface (>0.02 gm^{-3}). (See Figure 7d-e.) In all, 10 out of 22 cases have RWC higher than $10^{-3} \mathrm{gm}^{-3}$ at the surface, 4 of which are on 9 February.

In contrast, one case on 4 February evaporates completely within 400 m from the cloud base with no rain reaching the surface. This is because all drops in the RSD for this case are smaller than $300 \mu m$ (Figure 3a), and smaller drops are more

susceptible to evaporation. The cases on 5 and 10 February have RWC ranging between those on 4 and 9 February, with rain intense enough to reach the surface after partial evaporation.

RWC decreases at a faster rate for cases with smaller RWC at the cloud base, like on 4 February. This leads to an increase of F_e near the cloud base compared to near the surface (Figure 7f). Conversely, cases with higher RWC at the cloud base like on 9 February have a slower rate of decrease in RWC near the cloud base. This is primarily due to the higher concentration of larger drops in these cases that evaporate the most as they reach closer to the surface.

3.3.2   Vertical distributions of N_0, D_g and σ

The modeled microphysical parameters N_0, D_g and σ are shown in Figure 7a-c, where 9 February cases have the highest cloud base N_0 (>1000 m^{-3}). The decrease in N_0 with decreasing altitude corresponds well with that in RWC seen earlier.

The net modeled D_g increases and σ decreases from the cloud base to the surface across all the 22 P3 cases. Changes in D_g and σ are much smaller than in N_0. In general, D_g increases and σ decreases whenever smaller drops in the RSD evaporate completely. In this way, the complete evaporation of smaller drops makes the RSD narrower and centered over larger D_g. In contrast, if the RSD only has larger drops that only partially evaporate, then the D_g decreases and σ increases making the RSD wider and centered over smaller D_g.

The higher terminal velocity for bigger drops helps them reach the surface faster, while the longer residence time of slower-falling smaller drops in the sub-cloud layer leads to more complete evaporation of those drops. Thus the lower terminal velocity aids in the overall shift of the RSD towards larger D_g, narrower σ, and lower N_0 from the cloud base to the surface.

3.3.3   Sub-cloud stability due to the vertical distribution of F_e

How bottom- or top-heavy a profile of F_e is may have an effect on the boundary layer stability. For example, if most moisture from the rain evaporation is closer to the cloud base than to the surface (top-heavy profile), then the evaporation-cooled air near the cloud base could mix with the surface-based relatively warmer air more readily. This could potentially help in circulating the surface moisture to the cloud base and help the cloud stay intact.

In contrast, a bottom-heavy rain evaporation profile, where the maximum evaporation-produced moisture is concentrated close to the surface could lead to a stable configuration. This is because the cooler air close to the surface is not invigorated to mix with the relatively warmer air close to the cloud base. This could inhibit any mixing or vertical transport of moisture from the surface to the cloud base. Such profiles should be more susceptible to cloud dissipation and boundary layer decoupling and may promote the formation of cold pools. Examples of such top- and bottom- heavy profiles, with their relation to boundary layer stability are discussed in Paluch and Lenschow (1991). In this study, we have used the modeled F_e profiles to differentiate between top- and bottom- heavy profiles.

To assess which of the 22 P3 cases are top- or bottom-heavy, we have summed up F_e over the bottom 350 m (surface to 350 m altitude) and the top 350 m (350-700 m altitude) to obtain F_{top} and F_{bottom}, respectively. The ratio of F_{bottom}/F_{top} for all the cases is calculated (Figure 9). F_{bottom}/F_{top}>1 denotes bottom-heavy profiles and F_{bottom}/F_{top}<1 top-heavy profiles. All the cases on 4 February and one on 5 February where most of the rain evaporated within 100 m from the cloud base have

F_{bottom}/F_{top} of 0-0.2 and are therefore top-heavy. In total, 11 out of 22 cases have a top-heavy profile, making it more likely for these cloud layers to remain connected with the surface layer.

Next, we evaluate which microphysical conditions are more likely to generate a top- or bottom- heavy F_e profile. Since the F_e structure is dependent on the microphysical state at cloud base, F_{bottom}/F_{top} should also be dependent on the microphysical parameters N_0, D_g and σ. To demonstrate this here, we have determined the correlation of N_0, D_g, and σ at cloud base with F_{bottom}/F_{top} for each case (Figure 9). A strong correlation is found between F_{bottom}/F_{top} and D_g and σ. Comparatively, F_{bottom}/F_{top} and N_0 correlate weakly. This might be because the net effect of N_0 gets canceled in the numerator and denominator of F_{bottom}/F_{top}. In all, over the 22 cases, the bottom-heavy sub-cloud profiles, which could be prone to cloud breakup and boundary layer decoupling, have higher D_g and σ at the cloud base. Conversely, the top-heavy profiles, that could facilitate more intact clouds and higher mixing with the surface layer, have smaller D_g and σ at the cloud base.

A lower RH_{sf} is also modeled to produce more top-heavy profiles (smaller F_{bottom}/F_{top}), and vice-versa (Figure 9). This is because the lower the RH_{sf} is, the faster the evaporation rate of drops, leading to the accumulation of moisture and latent flux closer to the cloud base and thus a top-heavy profile.

In summary, high D_g, σ, and RH_{sf} are all linked to a bottom-heavy energy profile and vice-versa. This shows how the microphysical and thermodynamic parameters of the sub-cloud layer are associated with changing the vertical energy structure and potentially, therefore, affecting the sub-cloud stability.

3.3.4   Microphysical and thermodynamic influence on F_{eT} and REF

REF in the sub-cloud layer is useful to determine the amount of rain reaching the surface and to formulate the amount of F_{eT}. F_{eT}, on the other hand, is an estimate of the column total rain evaporation flux generated in the sub-cloud layer, that could indicate the average evaporative cooling rate of the sub-cloud layer. Both REF and F_{eT} depend on the microphysical and thermodynamic processes in the cloud and sub-cloud layer, as shown by the following model results:

a) Microphysical influence: REF is a strong function of D_g and σ (correlation coefficient=-0.7 and -0.8 respectively). The higher the D_g and σ at the cloud base, the smaller the REF (Figure A1f,h). This is because a higher D_g and σ at the cloud base signifies an RSD with a high proportion of bigger raindrops that are more likely to reach the surface without completely evaporating. Conversely, smaller D_g and σ at the cloud base have higher modeled REF, since smaller drops evaporate more efficiently reducing the overall mass of the rain more. The influence of N_0 on REF is smaller compared to D_g and σ (Figure A1d). This is because when REF is expanded in terms of N_0, D_g, and σ, the N_0 appears in the numerator and denominator and almost cancels out.

F_{eT}, on the other hand, is strongly impacted by N_0 (as well as D_g and σ). This is because F_{eT} is proportional to N_0. In short, while the influence of N_0 is not prominent in REF, its influence dominates F_{eT}. Most of the P3 cases with higher D_g and σ also have higher N_0. Due to this, lower REF cases are mostly correlated with higher F_{eT}. But in some cases like on 9 February, D_g and σ are small but N_0 is large, leading to large REF and large F_{eT}. Similarly, two cases on 10 February, have large D_g and σ but small N_0, leading to small REF and small F_{eT}. Overall, the link between REF and F_{eT} may not be linear

due to the underlying microphysical processes. More microphysical observations over shallow rain datasets are required to affirm this connection in a robust way.

370   **b) Thermodynamic influence**: The correlation of REF with RH_{sf} is not as strong as with the microphysical parameters (Figure A1a-b). But in a sensitivity study, where the microphysical parameters are fixed and RH_{sf} is varied in 10% interval jumps, a lower RH_{sf} is correlated with higher REF (Figure 10), and vice-versa. Accordingly, change in RH_{sf} is a contributing factor in changing REF.

    F_{eT} also increases as RH_{sf} decreases. As RH_{sf} decreases and the sub-cloud layer becomes drier, the rate of change in drop

375 size increases ($\frac{dD}{dz}$ in Equation 1). The sensitivity test suggests that for every 10% increase in RH_{sf}, F_{eT} decreases by $\approx$2-6 Wm^{-2}. For 17 out of 22 cases, RH_{sf} is between 67-74%. The rest of the 5 cases are on 5 February and have higher RH_{sf} of 76-87%. Holding the microphysical parameters constant, an increase in RH_{sf} from 67% to 87% would decrease REF and F_{eT} by 60% and 53%, respectively.

3.3.5 F_{eT} vs $F_{p,cb}$

380 A scatter plot between $F_{p,cb}$ and F_{eT} is shown for 20 of the 22 cases (Figure 9a). The other two cases are from 9 February where $F_{p,cb}$ is higher than 500 Wm^{-2} and are not shown in the figure for clarity. Five out of the 22 cases on 4 and 5 February, where rain evaporates completely, have F_{eT} equal to $F_{p,cb}$. Otherwise, as $F_{p,cb}$ increases, F_{eT}, and hence REF, tend to become smaller.

    The slope of $F_{p,cb}$ versus F_{eT} shown in Figure 9a is 0.63, indicating that on average 63% of the rain mass sampled by the P3

385 has evaporated in the sub-cloud layer. The magnitude of F_{eT} is between 15-352 Wm^{-2} for 9 out of 22 cases. This is analogous to 2-50 K/day of net evaporative cooling rate for the sub-cloud layer, estimated using $\frac{\delta T}{\delta t} = \frac{1}{\rho_a c_p} \frac{F_{eT}}{H}$, with ρ_a, c_p and H as density of air, heat capacity of dry air and cloud base height. This is comparable to a typical longwave radiative cooling rate over the marine boundary layer depth of 4-10 K/day and therefore should significantly contribute to the boundary layer energy budget in shallow convective environments where rain is present.

390 ## 3.4   Rain evaporation analysis using rain isotope ratios δD_p and $\delta^{18}O_p$

3.4.1   Modeled δD_p, $\delta^{18}O_p$ and d_p for the P3 cases

Changes in δD_p, $\delta^{18}O_p$ and d_p are modeled for all the 22 P3 cases (Figure 7g-i). As rain evaporates in the sub-cloud layer, the modeled δD_p and $\delta^{18}O_p$ increase, and d_p decreases towards the surface. The decrease in d_p is caused by the preferential evaporation of D in the water molecule owing to their lower mass, higher vapor pressure, and larger diffusivity compared to

395 ^{18}O, leaving the rain less enriched in δD_p compared to $\delta^{18}O_p$.

    The P3 cases with the higher modeled surface d_p have either high RH_{sf} (>75%) or large D_g and σ (compared to average P3 values), or both. The model also shows a positive correlation between the fractional change in d_p from cloud base to the surface (1-$d_{p,sf}/d_{p,cb}$) and REF for the 22 P3 cases (Figure 8). This is logical since a small REF suggests less fraction of rain mass evaporation which would correspond to a smaller change in d_p from the cloud base to the surface.

3.4.2 Comparison of model results with surface δD_p, $\delta^{18}O_p$ and d_p observations

The surface-based observations of δD_p, $\delta^{18}O_p$ (Figure A3) and d_p (Figure 11a) from the Brown, the BCO, and the Meteor range between 0-20‰, -2.5-1.2‰ and 4-18‰, respectively. δD_p for the BCO is slightly smaller than for the Brown and Meteor, and the Meteor d is slightly smaller compared to the BCO and the Brown. Overall, these values correspond well to those across other platforms during the EUREC^{4}A/ATOMIC campaign (refer to Bailey et al. (2023)). In particular, the rain sampled by the Brown shows surface rain rates of 1-5 mm/hr at an average RH_{sf} of 85%. These values are higher compared to the average P3 rain rate and RH_{sf}.

The modeled d_p at the surface for the P3 cases are between -2 to 9 ‰ (Figure 11b, blue line). Of these, the cases with RH_{sf} higher than 73% have the higher d_p between 3-9 ‰. These higher modeled d_p cases overlap with some of the Brown observations of 8-18 ‰. Moreover, when all the P3 cases are run at an increased RH_{sf} of 85% to replicate the Brown thermodynamic conditions, the modeled surface d_p increases to 6-10 ‰ (Figure 11b, red line). This finding is consistent with the idea that we would expect measurable rain with higher d_p to reach the surface when RH_{sf} is higher.

Similarly, the modeled d_p also shifts closer to the Brown values when the model is run at larger D_g and σ compared to the P3 ranges. Running the model at D_g to 0.5 mm and RH_{sf} of 85%, and keeping σ within the P3 range (1-2.5), the modeled surface d_p increases to 8-13 ‰ (Figure 11b, yellow line). Further, increasing σ to 3 along with D_g and RH_{sf}, also further increases the modeled d_p to 14‰ (Figure 11b, purple line). The choice of increasing σ to 3 is consistent with the upper range of σ during RICO (Figure 4 in Geoffroy et al. (2014)).

A higher D_g and σ at the cloud base lead to a lower fraction of rain mass evaporation or lower REF. A lower REF then leads to less change in d_p between the cloud base and surface and hence larger surface d_p. The evaluation of the model outputs against the station observations also lends credibility to our model. These experiments demonstrate the strong thermodynamic and microphysical influence of the sub-cloud layer on the surface d_p. Equivalently, the reliability of using d_p as a metric for sub-cloud rain evaporation studies is also demonstrated.

Note that both δ_p and d_p are independent of N_0, and only depend on D_g and σ. This can explain why an 'amount effect' (Dansgaard, 1964) is not always present in low-latitude isotopic datasets. The amount effect suggests that for a given rain sample, if the rain rate is high, then δ_p should be low, and vice versa. However, this may not always hold true for all microphysical conditions. If N_0 is large and D_g and σ are small, the rain rate could still be high due to its strong sensitivity to N_0. But, due to the small D_g and σ, the δ_p will also be high. Similarly, if N_0 is small and D_g and σ are large, then both the rain rate and δ_p will be low. Consequently, the amount effect may not be appropriate for explaining all rain events, especially when the microphysical variability is pronounced.

3.5 Water vapor isotope ratio variations

Next, we assess whether raindrop evaporation during the P3 cases could cause a detectable isotopic change in the sub-cloud layer water vapor. The maximum simulated F_e, associated with 9 February, was 0.7 $Wm^{-2}m^{-1}$, which corresponds to a moisture flux of $3.1x10^{-4}$ $g/m^3/s$ ($\frac{F_e}{L}$). Over the course of a 15-minute rain shower, and neglecting dilution or advection, this

flux would cause a change in absolute humidity of about 0.3 g/m^3 ($\frac{F_e \times 900s}{L}$). Since the measured absolute humidity on this day was 15 g/m^3, these results indicate that rain evaporation may have contributed 2% to the moisture content of the sub-cloud layer. Given the observed δD_v of -71 ‰ and the simulated δD_e of 5 ‰, we can estimate the isotopic change in sub-cloud layer water vapor due to raindrop evaporation from Equation 11, which yields an isotopic change of 1 ‰. Since variations of 1 ‰ δD_v are readily detectable with today's airborne water vapor isotopic analyzers, we surmise that rain on 9 February should have caused a measurable shift in the water vapor isotope ratios of the sub-cloud layer.

4   Conclusions and discussion

This study evaluates shallow rain evaporation characteristics in the North Atlantic Ocean near Barbados using a one-dimensional sub-cloud rain evaporation model initialized by observations from the EUREC[4]A/ATOMIC campaign. The focus is on 22 raining cases sampled by the P3, where the cloud base leg mean rain rates and RWC are between 0.01-31 mm/day and 0.0001-0.1 gm^{-3}, respectively. These cases show interesting variability in their sub-cloud rain evaporation characteristics, as well as their dependence on the microphysical and thermodynamic state of the boundary layer.

The total rain evaporation flux (F_{eT}) over the 22 P3 cases is modeled to be 15-352 Wm^{-2}, which is close to the 3-day mean 100 Wm^{-2} latent heat flux at 200 m altitude that was measured remotely from aboard the Maria S. Merian, another EUREC[4]A research vessel that sampled to the south of the P3 study region (Stevens et al., 2021). The F_{eT} for the P3 cases are also comparable with estimates from ASTEX (42 Wm^{-2}), RICO (130 Wm^{-2}) and CSET (10-200 Wm^{-2}). These differences and variability, especially between the P3 cases and during RICO and CSET, are a result of differences in their RH$_{sf}$, D_g, σ and N_0 in the sub-cloud layer.

F_{eT} of 15-352 Wm^{-2} over a 700 m deep sub-cloud layer is equivalent to 2-50 K/day of evaporative cooling. This is comparable to the typical stratocumulus cloud top radiative longwave cooling (4-10 K/day) and with the rain evaporation cooling rate at cloud base in the marine sub-cloud stratocumulus deck of 2-20 K/day shown in Wood (2005). This shows that shallow rain evaporation can contribute significantly to the local energy budget and sub-cloud cooling rates.

Depending on the vertical distribution and magnitudes of F_e, the sub-cloud layer could be energetically top- or bottom-heavy and potentially influence the boundary layer stability through downdrafts or decoupling. Eleven out of the 22 cases have most of their rain evaporated closer to the surface. This 'bottom-heavy' configuration should inhibit mixing with the warmer air near the cloud base and, therefore, should aid the boundary layer in decoupling faster. This could also facilitate cold-pool formation.

In contrast, the other 11 cases that are 'top-heavy' accumulate moisture near the cloud base and are more prone to mixing with warmer air below. This could lead to a mixed boundary layer in which clouds could remain intact longer. A follow-up modeling study is needed to confirm these processes and to see the degree to which the boundary layer stability depends on the representation of rain evaporation within the model.

A top-heavy F_e profile is linked with lower D_g and σ at the cloud base. This makes physical sense since a lower D_g and σ at the cloud base would mean that the raindrops are small and the RSD is narrow enough for the drops to evaporate closer to

the cloud base. Conversely, a bottom-heavy F_e profile is linked with higher D_g and σ due to the higher concentration of larger drops that reach the surface without evaporating completely. This emphasizes the influence of microphysical characteristics of rain at cloud base on the sub-cloud vertical F_e profile.

Additionally, given constant microphysical parameters at the cloud base, a top-heavy F_e profile is also linked with lower RH$_{sf}$. This is because lower RH$_{sf}$ increases the rate of rain evaporation, especially for smaller drops, facilitating more accumulation of moisture close to the cloud base. In contrast, higher RH$_{sf}$ favors bottom-heavy F_e profiles. This depicts the influence of thermodynamic conditions, in addition to microphysical conditions, in modulating the vertical rain evaporation flux distribution.

The model also shows that, on average, 63% of the rain mass evaporated in the sub-cloud layer for the 22 P3 cases. Most of these cases with higher REF are associated with smaller D_g, σ and RH$_{sf}$, and vice-versa. However, the effect of RH$_{sf}$ on REF is lower compared to D_g and σ.

Moreover, if N_0, D_g, and σ are all large, then F_{eT} tends to be large and REF small, as seen for most of the 22 P3 cases. However, there are cases when D_g and σ are large but N_0 is small. This leads to small F_{eT} and small REF. A few cases also have small D_g and σ but large N_0, resulting in fairly large F_{eT} and large REF. Effectively, therefore, the fraction of rain evaporated (or REF) and the amount of rain evaporated (or F_{eT}), are more intrinsically dependent on the RSD microphysical parameters, rather than on the bulk RWC itself.

In terms of rain isotopic composition, our results show that sub-cloud conditions with higher RH$_{sf}$, higher D_g, and σ are prone to higher surface d_p. This is because a higher RH$_{sf}$ and higher cloud base D_g and σ lead to less evaporation of raindrops and low REF and, thereby, smaller changes in d_p between the cloud base and the surface. In general, REF varies linearly with the fractional change in d_p between the cloud base and the surface (or 1-$d_{p,sf}/d_{p,cb}$). Isotope differences in the rain between the cloud base and the surface thus provide an independent measure of REF.

The model results also suggest why the 'amount effect' or a negative correlation between rain rate and δ_p is not always found in low latitudes. It is a result of the underlying microphysics of the RSD. If the high rain rate is due to large D_g and σ, then the δ_p should be low due to small REF. In contrast, if the rain rate is high because of high N_0 and small D_g and σ, then δ_p should be high due to high REF. This is especially relevant for shallow rain regimes where microphysics plays a significant role in determining rain characteristics.

In general, our isotope-initialized microphysics-resolved model performs reliably well in characterizing the sub-cloud rain evaporation in the shallow rain regime sampled during the ATOMIC/EUREC^{4}A campaign. This model also only requires in-situ microphysical and rain isotope observations and is independent of any remotely-sensed rain observations. However, a comparison between rain evaporation evaluated from remote-sensing platforms (e.g., mm-wavelength radars) and our in-situ-based model could be useful for error analysis between different methods.

The results from the model emphasize the role of microphysical and thermodynamic processes in accurately simulating sub-cloud rain evaporation. The variability of the modeled rain evaporation fluxes across the 22 P3 cases also highlights the need for more samples in similar shallow cloud regimes for a more robust statistical interpretation that could be used to evaluate GCM parameterizations. The model also provides an opportunity to extend the rain evaporation study from other field campaigns

conducted over different ocean basins and different seasons, which is crucial for a wider understanding of sub-cloud rain processes.

Acknowledgements. This material is based upon work supported by the National Center for Atmospheric Research, which is a major facility sponsored by the National Science Foundation under Cooperative Agreement No. 1852977. The NSF support for the EUREC^{4}A-Iso campaign is from NSF grant No. 1937780. PNB's contribution to this work was supported by the National Science Foundation under Grant AGS-1938108. We acknowledge the entire team of ATOMIC/EUREC^{4}A for collecting and processing the data from all the platforms used in this study. We thank the two internal reviewers at NCAR and two anonymous external reviewers for their thoughtful comments.

Data availability. The description of the campaign is cataloged at https://psl.noaa.gov/atomic. The doi for all the processed datasets is available at https://psl.noaa.gov/atomic/data/.

Author contributions. MS, and AB designed the study. MS performed the analysis and wrote the paper. AB, PB, SPD, DN and EQM revised the paper, and provided useful feedback on the Figures and text. EQM processed the Ron Brown isotope datasets. MDL and PYC collected all of the P3 microphysical datasets. MDL stitched the CIP and PIP microphysical datasets for all the flights.

Competing interests. There are no competing interests.

Code availability. The one-dimensional steady-state rain evaporation code used for this analysis and written in MATLAB is attached.

References

Albrecht, B., Ghate, V., Mohrmann, J., Wood, R., Zuidema, P., Bretherton, C., Schwartz, C., Eloranta, E., Glienke, S., Donaher, S., Sarkar, M., McGibbon, J., Nugent, A., Shaw, R. A., Fugal, J., Minnis, P., Palikonda, R., Lussier, L., Jensen, J., Vivekanandan, J., Ellis, S., Tsai, P., Rilling, R., Haggerty, J., Campos, T., Stell, M., Reeves, M., Beaton, S., Allison, J., Stossmeister, G., Hall, S., and Schmidt, S.: Cloud system evolution in the trades CSET following the evolution of boundary layer cloud systems with the NSF-NCAR GV, Bull. Am. Meteorol. Soc., p. 93–121, https://doi.org/10.1175/BAMS-D-17-0180.1, 2019.

Bailey, A., Aemisegger, F., Villiger, L., Los, S. A., Reverdin, G., Quiñones Meléndez, E., Acquistapace, C., Baranowski, D. B., Böck, T., Bony, S., et al.: Isotopic measurements in water vapor, precipitation, and seawater during EUREC 4 A, Earth System Science Data, 15, 465–495, 2023.

Bretherton, C. S. and Pincus, R.: Cloudiness and marine boundary layer dynamics in the ASTEX Lagrangian experiments. Part I: Synoptic setting and vertical structure, Journal of Atmospheric Sciences, 52, 2707–2723, https://doi.org/10.1175/1520-0469(1995)052<2707:CAMBLD>2.0.CO;2, 1995.

Byers, H. R. and Hall, R. K.: A census of cumulus-cloud height versus precipitation in the vicinity of Puerto Rico during the winter and spring of 1953-1954, Journal of the Atmospheric Sciences, 12, 176–178, https://doi.org/10.1175/1520-0469(1955)012<0176:ACOCCH>2.0.CO;2, 1955.

Caldwell, P., Bretherton, C. S., and Wood, R.: Mixed-layer budget analysis of the diurnal cycle of entrainment in southeast Pacific stratocumulus, Journal of Atmospheric Sciences, 62, 3775–3791, https://doi.org/10.1175/JAS3561.1, 2005.

Dansgaard, W.: Stable isotopes in precipitation, tellus, 16, 436–468, https://doi.org/10.1111/j.2153-3490.1964.tb00181.x, 1964.

de Szoeke, S. P., Skyllingstad, E. D., Zuidema, P., and Chandra, A. S.: Cold pools and their influence on the tropical marine boundary layer, Journal of the Atmospheric Sciences, 74, 1149–1168, https://doi.org/10.1175/JAS-D-16-0264.1, 2017.

Fairall, C. W., Matrosov, S. Y., Williams, C. R., and Walsh, E. J.: Estimation of Rain Rate from Airborne Doppler W-Band Radar in CalWater-2, J. Atmos. Oceanic Technol., 35, 593–608, https://doi.org/10.1175/JTECH-D-17-0025.1, 2018.

Feingold, G. and Levin, Z.: The lognormal fit to raindrop spectra from frontal convective clouds in Israel, Journal of climate and applied meteorology, pp. 1346–1363, 1986.

Galewsky, J. and Los, S. A.: M161 Rainwater Isotopic Composition [Dataset], Aeris, https://doi.org/10.25326/308, 2020.

Geoffroy, O., Siebesma, A. P., and Burnet, F.: Characteristics of the raindrop distributions in RICO shallow cumulus, Atmos. Chem. Phys., 14, 10 897–10 909, https://doi.org/10.5194/acp-14-10897-2014, 2014.

Graf, P.: The effect of below-cloud processes on short-term variations of stable water isotopes in surface precipitation, Ph.D. thesis, ETH Zurich, https://doi.org/10.3929/ethz-b-000266387, 2017.

Graf, P., Wernli, H., Pfahl, S., and Sodemann, H.: A new interpretative framework for below-cloud effects on stable water isotopes in vapour and rain, Atmospheric chemistry and physics, 19, 747–765, https://doi.org/10.5194/acp-19-747-2019, 2019.

Jensen, J. B., Lee, S., Krummel, P. B., Katzfey, J., and Gogoasa, D.: Precipitation in marine cumulus and stratocumulus.: Part I: Thermodynamic and dynamic observations of closed cell circulations and cumulus bands, Atmospheric Research, 54, 117–155, https://doi.org/10.1016/S0169-8095(00)00040-5, 2000.

Kalmus, P., Lebsock, M., and Teixeira, J.: Observational boundary layer energy and water budgets of the stratocumulus-to-cumulus transition, Journal of Climate, 27, 9155–9170, https://doi.org/10.1175/JCLI-D-14-00242.1, 2014.

Leandro, M. and Chuang, P.: Size-resolved cloud and aerosol number concentrations taken from N43 aircraft in the North Atlantic Ocean, Barbados: Atlantic Tradewind Ocean-Atmosphere Mesoscale Interaction Campaign 2020-01-31 to 2020-02-10 (NCEI Accession 0232458), (Dataset), https://doi.org/10.25921/vwvq-5015, 2021.

Majoube, M.: Fractionnement en oxygène 18 et en deutérium entre l'eau et sa vapeur, Journal de Chimie Physique, 68, 1423–1436, https://doi.org/10.1051/jcp/1971681423, 1971.

Mohrmann, J., Bretherton, C. S., McCoy, I. L., McGibbon, J., Wood, R., Ghate, V., Sarkar, M., Zuidema, P., Albrecht, B. A., and Palikonda, R.: Lagrangian evolution of the Northeast Pacific marine boundary layer structure and cloud during CSET, Mon. Wea. Rev., 147, 4681–4700, https://doi.org/10.1175/MWR-D-19-0053, 2019.

Nicholls, S. and Leighton, J.: An observational study of the structure of stratiform cloud sheets: Part I. Structure, Quarterly Journal of the Royal Meteorological Society, 112, 431–460, https://doi.org/10.1002/qj.49711247209, 1986.

Noone, D.: Pairing measurements of the water vapor isotope ratio with humidity to deduce atmospheric moistening and dehydration in the tropical midtroposphere, Journal of Climate, 25, 4476–4494, https://doi.org/10.1175/JCLI-D-11-00582.1, 2012.

O, K.-T., Wood, R., and Bretherton, C.: Ultraclean Layers and Optically Thin Clouds in the Stratocumulus-to-Cumulus Transition. Part II: Depletion of Cloud Droplets and Cloud Condensation Nuclei through Collision–Coalescence, J. Atmos. Sci., 75, 1653–1673, https://doi.org/10.1175/JAS-D-17-0218.1, 2018.

Paluch, I. R. and Lenschow, D. H.: Stratiform cloud formation in the marine boundary layer, J. Atmos. Sci., 48, 2141–2158, https://doi.org/10.1175/1520-0469(1991)048<2141:SCFITM>2.0.CO;2, 1991.

Pincus, R., Fairall, C. W., Bailey, A., Chen, H., Chuang, P. Y., De Boer, G., Feingold, G., Henze, D., Kalen, Q. T., Kazil, J., et al.: Observations from the NOAA P-3 aircraft during ATOMIC, Earth System Science Data, 13, 3281–3296, https://doi.org/10.5194/essd-13-3281-2021, 2021.

Pruppacher, H., Klett, J., Pruppacher, H., and Klett, J.: Microstructure of atmospheric clouds and precipitation, Microphysics of clouds and precipitation, pp. 10–73, 2010.

Quinn, P. K., Thompson, E. J., Coffman, D. J., Baidar, S., Bariteau, L., Bates, T. S., Bigorre, S., Brewer, A., de Boer, G., de Szoeke, S. P., et al.: Measurements from the RV Ronald H. Brown and related platforms as part of the Atlantic Tradewind Ocean-Atmosphere Mesoscale Interaction Campaign (ATOMIC), Earth System Science Data, 13, 1759–1790, https://doi.org/10.5194/essd-13-1759-2021, 2021.

Risi, C., Muller, C., and Blossey, P.: What controls the water vapor isotopic composition near the surface of tropical oceans? Results from an analytical model constrained by large-eddy simulations, Journal of Advances in Modeling Earth Systems, 12, e2020MS002 106, https://doi.org/10.1029/2020MS002106, 2020.

Salamalikis, V., Argiriou, A., and Dotsika, E.: Isotopic modeling of the sub-cloud evaporation effect in precipitation, Science of the Total Environment, 544, 1059–1072, https://doi.org/10.1016/j.scitotenv.2015.11.072, 2016.

Sandu, I. and Stevens, B.: On the Factors Modulating the Stratocumulus to Cumulus Transitions, J. Atmos. Sci., 68, 1865–1881, https://doi.org/10.1175/2011jas3614.1., 2011.

Sarkar, M., Zuidema, P., Albrecht, B., Ghate, V., Jensen, J., Mohrmann, J., and Wood, R.: Observations pertaining to precipitation within the Northeast Pacific Stratocumulus-to-Cumulus Transition, Mon. Wea. Rev., https://doi.org/10.1175/MWR-D-19-0235.1., 2020.

Sarkar, M., Zuidema, P., and Ghate, V.: Clarifying Remotely Retrieved Precipitation of Shallow Marine Clouds from the NSF/NCAR Gulfstream V, Journal of Atmospheric and Oceanic Technology, 38, 1657–1670, https://doi.org/10.1175/JTECH-D-20-0166.1, 2021.

Schwartz, M. C., Ghate, V. P., Albrecht, B. A., Zuidema, P., Cadeddu, M., Vivekanandan, J., Ellis, S. M., Tsai, P., Eloranta, E. W., Mohrmann, J., Wood, R., and Bretherton, C. S.: Merged Cloud and Precipitation Dataset from the HIAPER-GV for the Cloud System Evolution in the Trades CSET Campaign, J. Atmos. Ocean. Technol., https://doi.org/10.1175/jtech-d-18-0111.1, 2019.

590   Seifert, A.: On the parameterization of evaporation of raindrops as simulated by a one-dimensional rainshaft model, Journal of the Atmospheric Sciences, 65, 3608–3619, 2008.

Short, D. A. and Nakamura, K.: TRMM radar observations of shallow precipitation over the tropical oceans, Journal of Climate, 13, 4107–4124, https://doi.org/10.1175/1520-0442(2000)013<4107:TROOSP>2.0.CO;2, 2000.

Snodgrass, E. R., Di Girolamo, L., and Rauber, R. M.: Precipitation characteristics of trade wind clouds during RICO de-
595   rived from radar, satellite, and aircraft measurements, Journal of Applied Meteorology and Climatology, 48, 464–483, https://doi.org/10.1175/2008JAMC1946.1, 2009.

Srivastava, R.: A simple model of evaporatively driven dowadraft: Application to microburst downdraft, Journal of Atmospheric Sciences, 42, 1004–1023, 1985.

Stevens, B.: Atmospheric moist convection, Annu. Rev. Earth Planet. Sci., 33, 605–643, https://doi.org/10.1146/annurev.earth.33.092203.122658,
600   2005.

Stevens, B., Bony, S., Farrell, D., Ament, F., Blyth, A., Fairall, C., Karstensen, J., Quinn, P. K., Speich, S., Acquistapace, C., et al.: EUREC4A, Earth System Science Data, 13, 4067–4119, https://doi.org/10.5194/essd-13-4067-2021, 2021.

Villiger, L., Herbstritt, B., Ringel, M., Stolla, M., Mech, M., Jansen, F., and Aemisegger, F.: Calibrated stable water isotope data in precipitation from the BCO during EUREC4A. [Dataset]. Aeris., https://doi.org/10.25326/242, 2021.

605   Wood, R.: Drizzle in stratiform boundary layer clouds. Part II: Microphysical aspects, J. Atmos. Sci., 62, 3023–3050, https://doi.org/10.1775/JAS-3530.1, 2005.

Worden, J., Noone, D., and Bowman, K.: Importance of rain evaporation and continental convection in the tropical water cycle, Nature, 445, 528–532, 2007.

Yamaguchi, T., Feingold, G., and Kazil, J.: Stratocumulus to Cumulus Transition by Drizzle, J. Adv. Model. Earth Syst., 9, 2333–2349,
610   https://doi.org/10.1002/2017MS001104, 2017.

Zuidema, P., Li, Z., Hill, R., Bariteau, L., Rilling, B., Fairall, C., Brewer, W. A., Albrecht, B., and Hare, J.: On tradewind cumulus cold pools, J. Atmos. Sci., 69, 258–277, https://doi.org/10.1175/jas-d-11-0143.1, 2012.
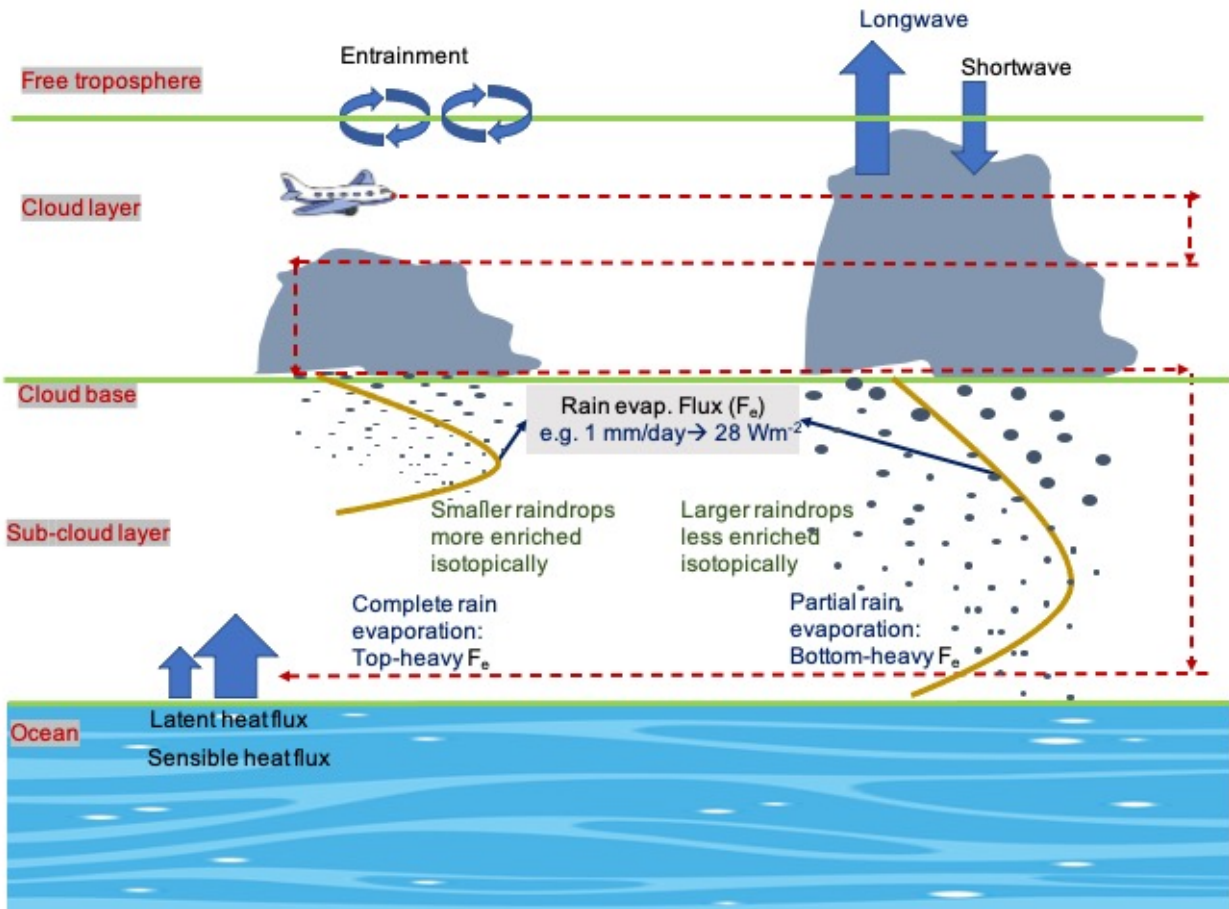
Figure 1. Schematic showing raining cumulus-topped boundary layer with the latent and sensible heat fluxes near the surface. The longwave and shortwave fluxes and free tropospheric entrainment mixing are shown at the cloud top. Rain can evaporate completely or partially as it falls toward the surface. This could lead to differences in vertical profiles of the rain evaporation fluxes depicted by the solid vertical curves. Complete evaporation of rain could cause the maximum rain evaporation flux close to the cloud base ('top-heavy') compared to partial evaporation which could bring the maxima closer to the surface ('bottom-heavy'). A 1 mm/day rain rate can potentially produce 28 Wm^{-2} of rain evaporation flux. The aircraft measurements are made at horizontal above-cloud, in-cloud, cloud base, and near-surface legs as shown by airplane cartoon and red dashed-line trajectories.
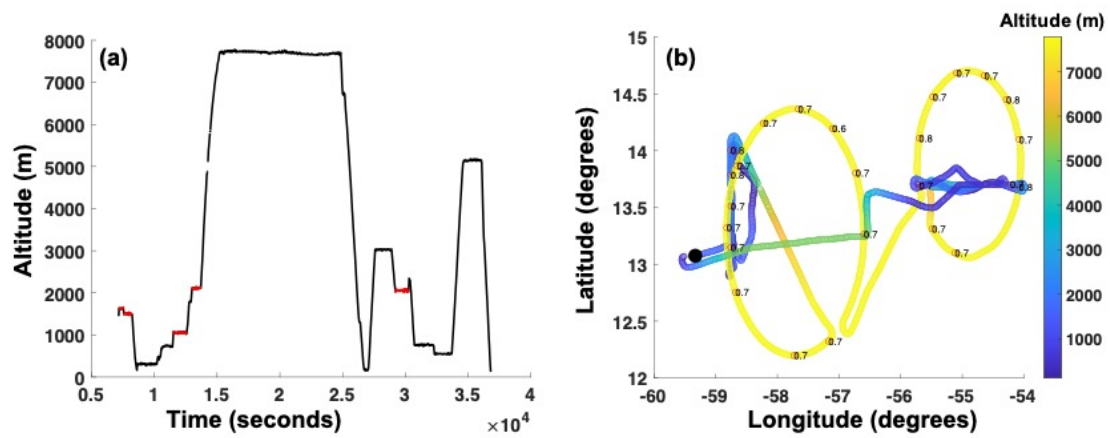
Figure 2. P3 trajectory on 9 February a) in time-altitude axes and b) in longitude-latitude axes with contour colors showing the altitude (in meters) of the P3. The red lines in a) denote the legs with mean rain rates greater than 0.01 mm/day that are selected for this study. Numbers in b) denote the surface relative humidity in a fraction of 1 over the dropsonde locations.
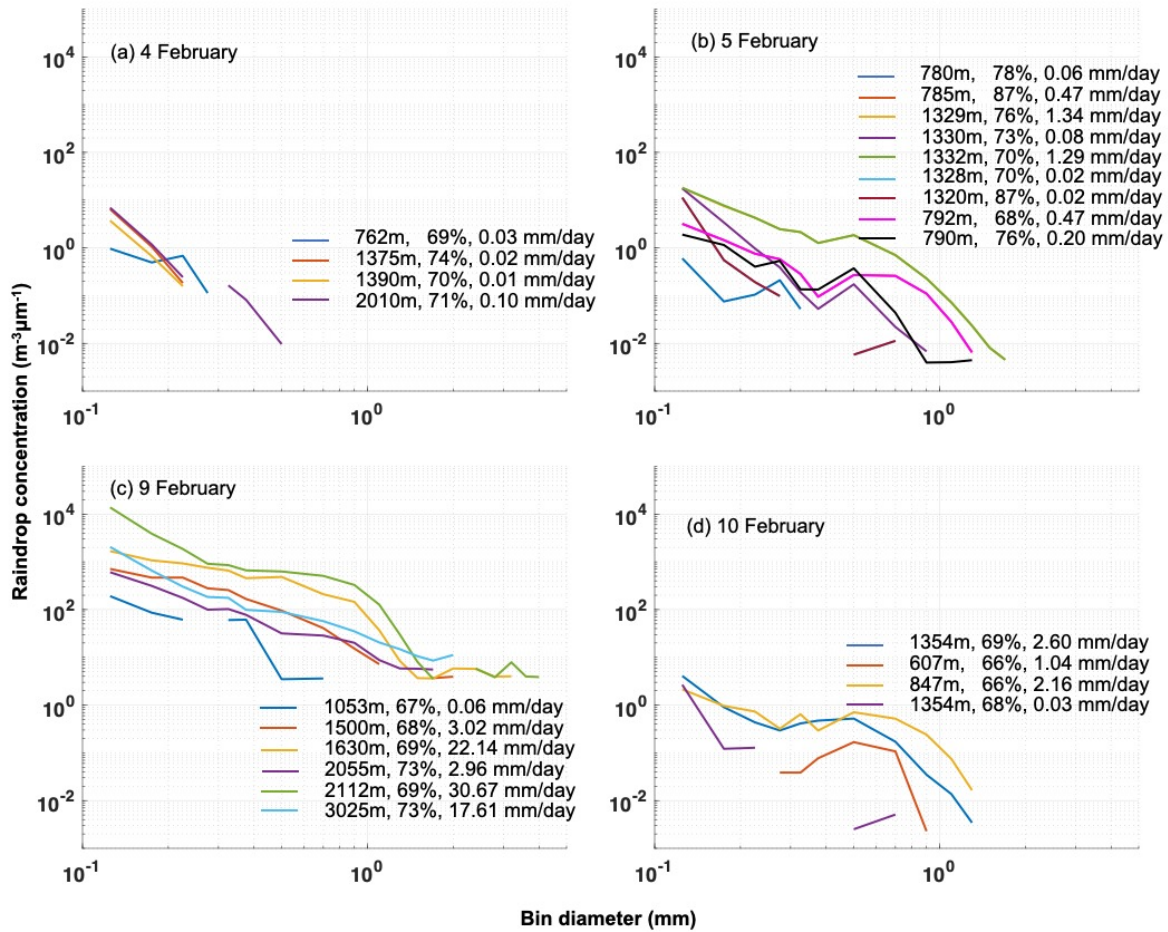
Figure 3. Raindrop size distribution is shown for 10-minute horizontal legs on a) 4 b) 5 c) 9 and d) 10 February. The legend shows the altitude of the horizontal legs, dropsonde-derived surface relative humidity, and leg-mean rain rates.
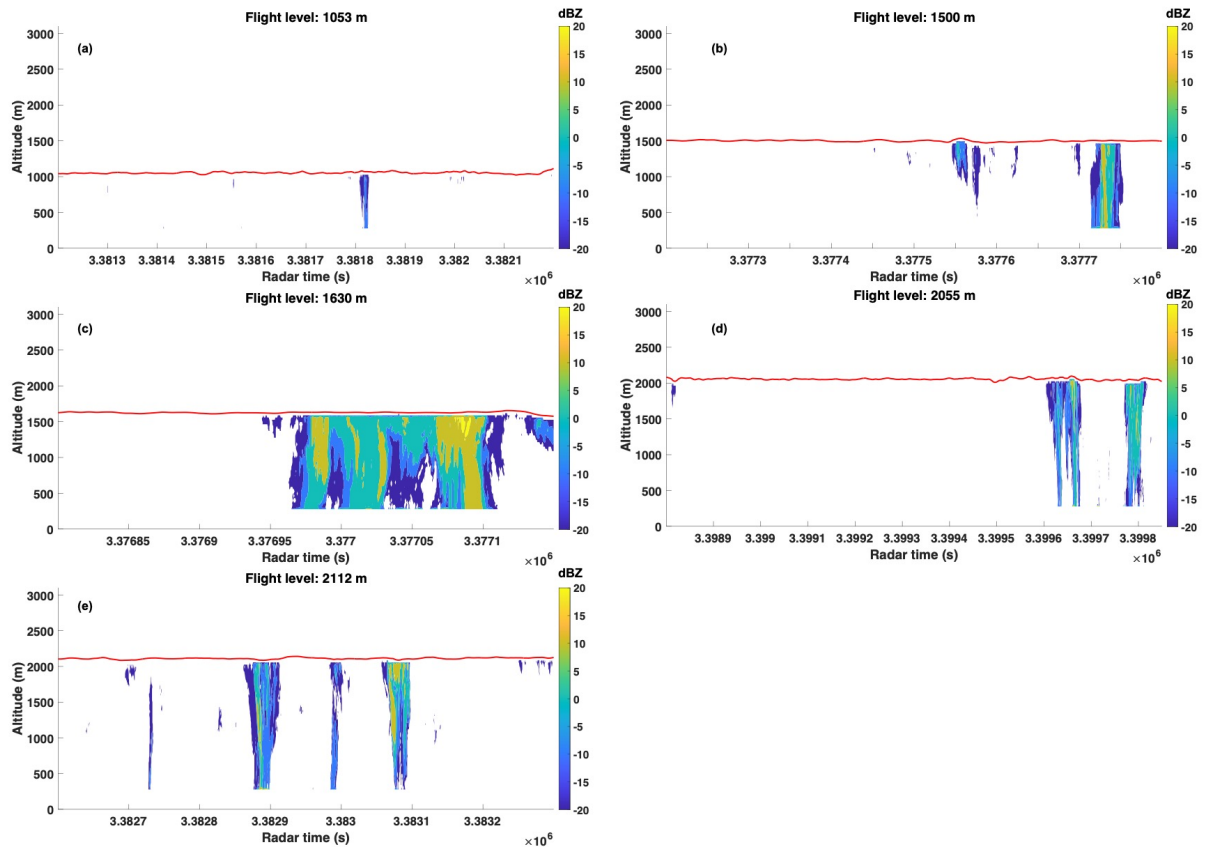
Figure 4. 94 GHz radar reflectivity (in dBZ) on board the P3 on 9 February pointing downwards for all the six horizontal level legs shown in Figure 2. The red line is the flight trajectory and the contour shade represents radar reflectivity.
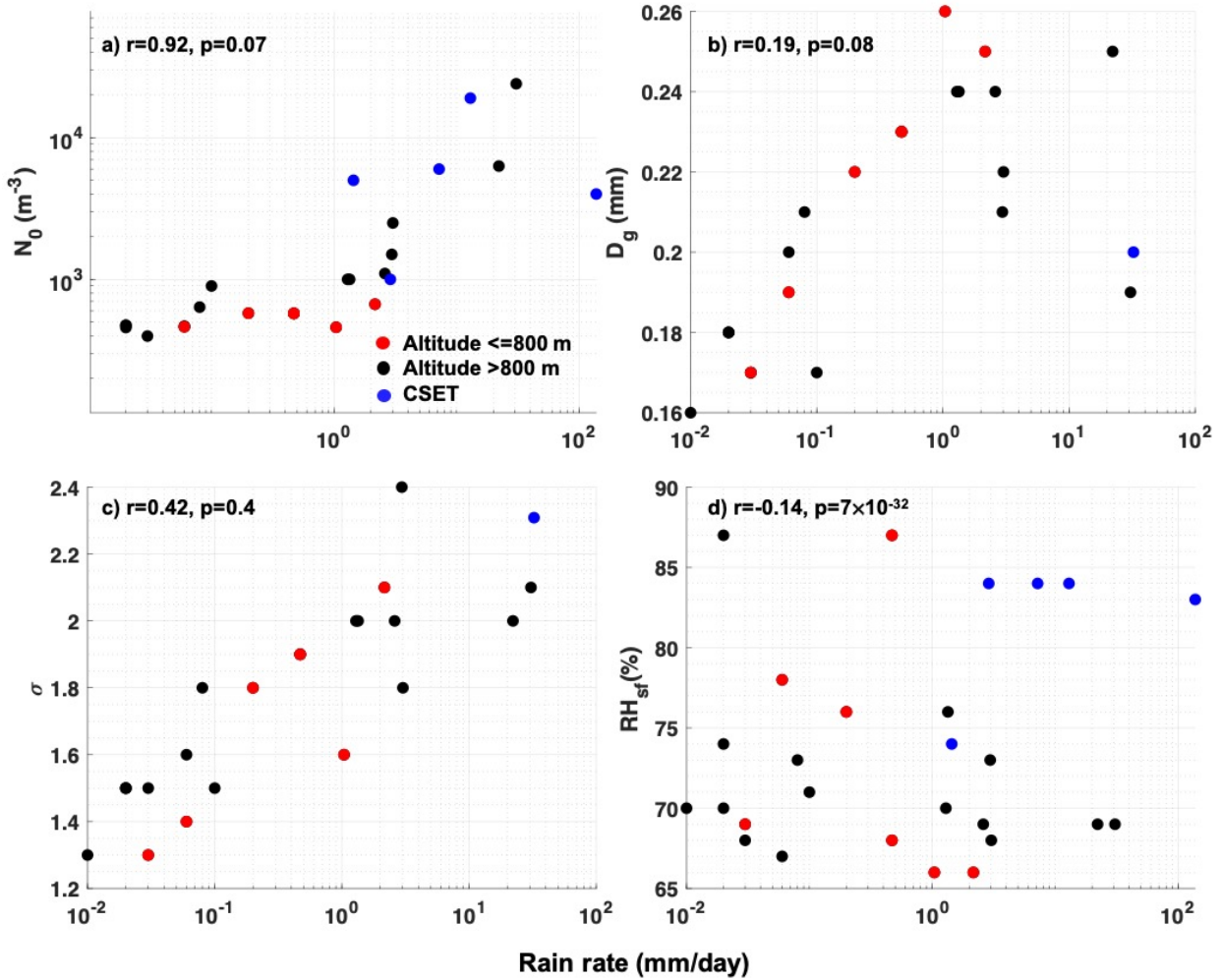
Figure 5. a) N_0, b) D_g, c) σ, and d) RH_{sf} are scattered against 10-minute leg mean rain rates for 22 cases observed by the P3. Red circles show the cases sampled at 700 ± 100 m altitude, and black circles are cases sampled at altitudes higher than 800 m. Blue circles are for the CSET campaign obtained from Sarkar et al. (2020). Only the average D_g and σ over five CSET cases were available and are shown by single dots in b-c). N_0 and RH_{sf} were available for five cases during CSET and are shown in a) and d). The correlation coefficients (r) and p-value are mentioned in all figures.
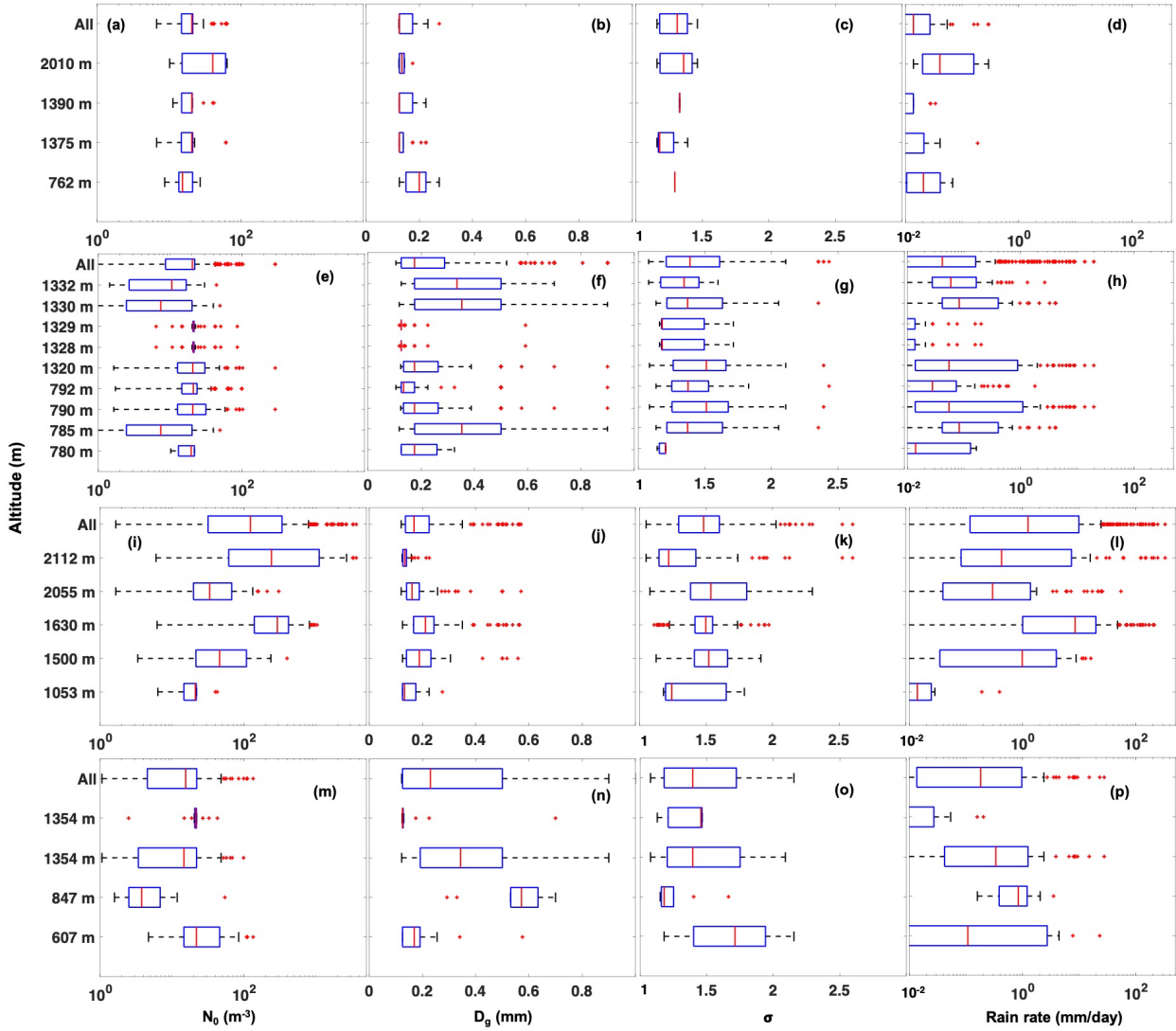
Figure 6. Lognormally fitted 1-Hz rain parameters (a,e,i,m) N_0, (b,f,j,n) D_g, (c,g,k,o) and σ and (d,h,l,p) rain rates are depicted as box-plots for all the 22 cases on (a-d) 4 Feb, (e-h) 5 Feb, (i-l) 9 Feb and (m-p) 10 Feb. The box plots denote the 25th, 50th, and 75th percentiles. The minimum and maximum extents of the whiskers denote the minimum and maximum data points that are not an outliers. Outliers are shown in red '+' symbols. Outliers are considered data points outside the +/-2.7×standard deviation and 99.3 percent coverage.
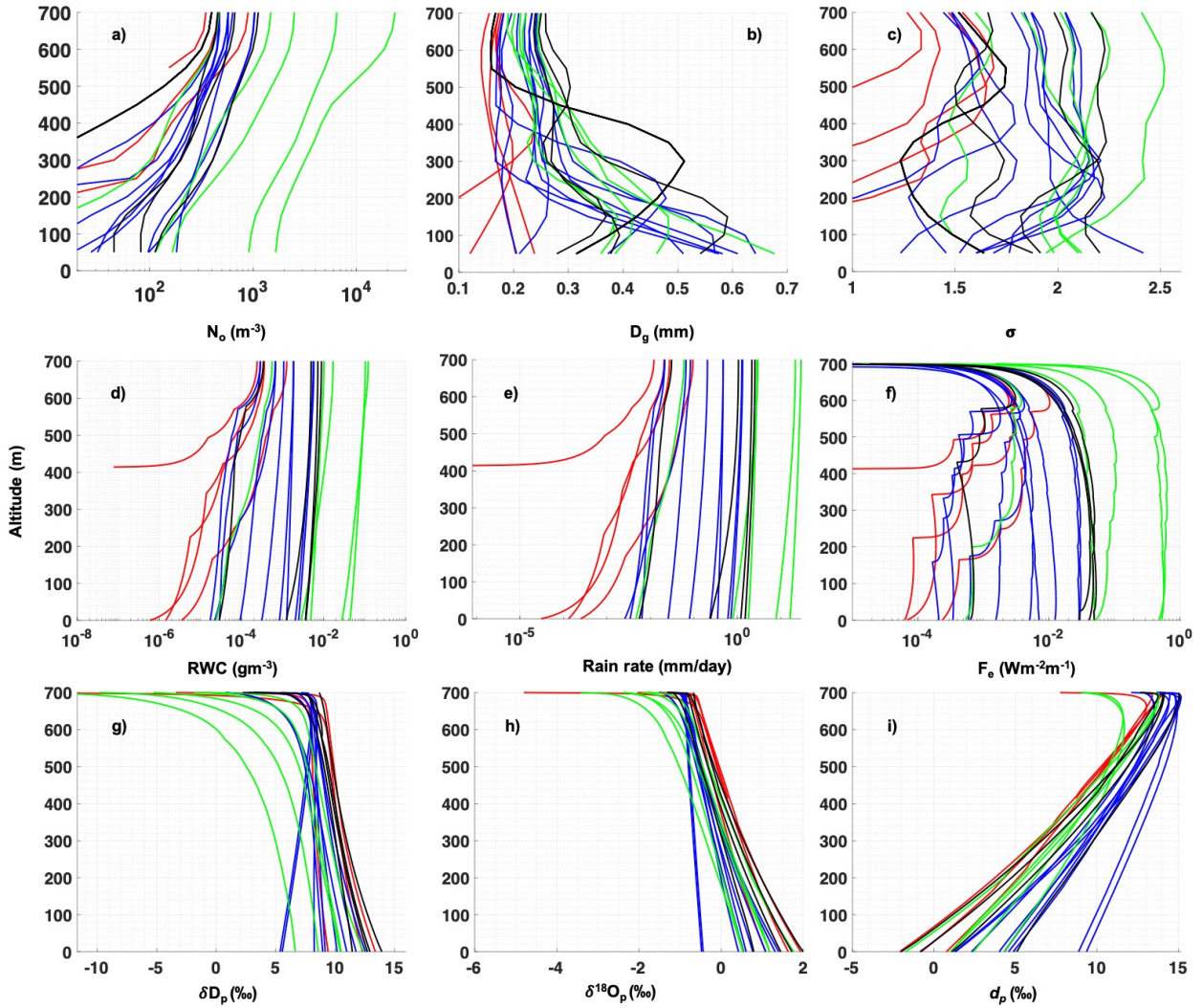
Figure 7. Modeled a)N_0, b)D_g, c)σ, d)RWC, e)Rain rate, f) F_e, g) $\delta^{18}O_p$, h) δD_p, and i) d_p vs. height for all the 22 P3 cases. 4, 5, 9, and 10 February cases are shown in red, blue, green, and black lines respectively. The modeled RSD is averaged over every 50 m vertical length and then fitted using lognormal distribution to obtain smooth N_0, D_g, and σ vertical profiles.
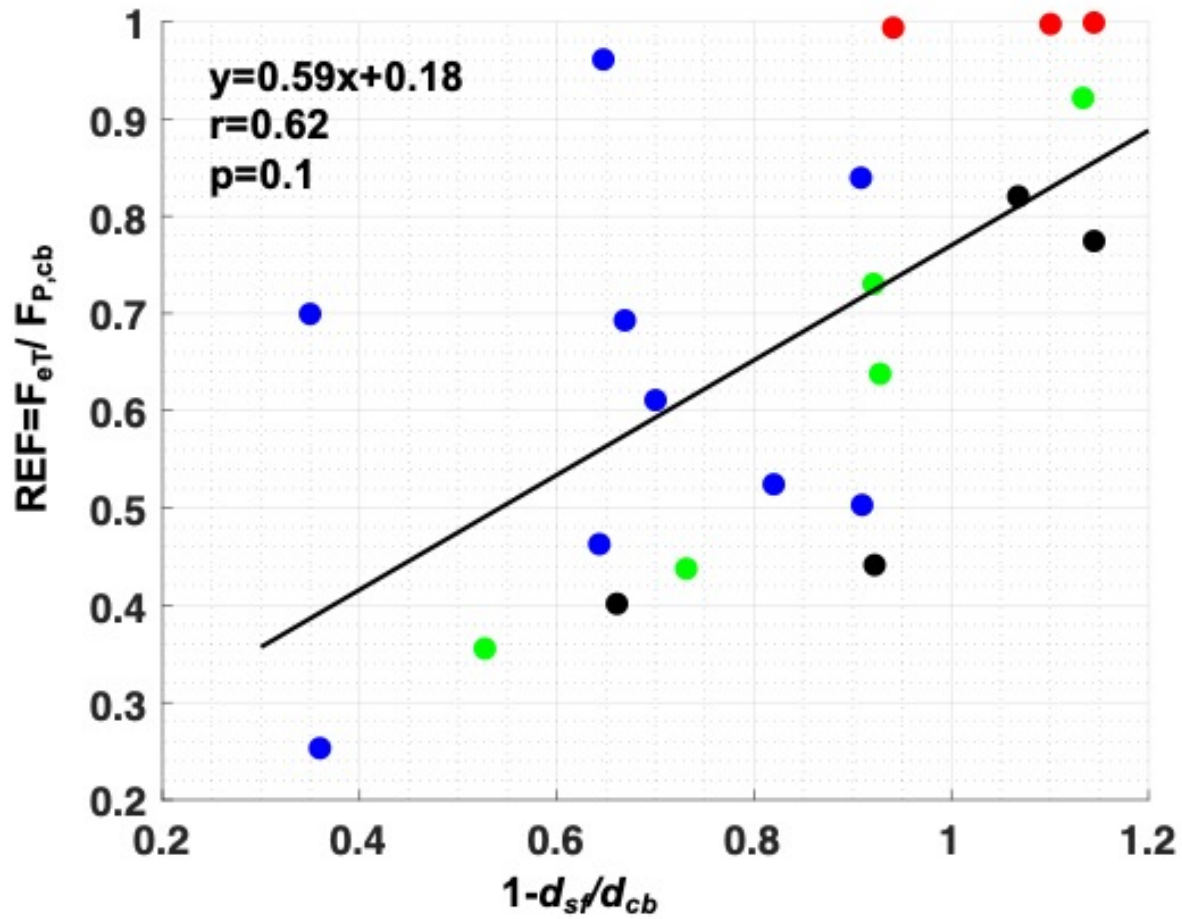
Figure 8. Modeled REF (=$F_{eT}/F_{p,cb}$) scattered along the fraction of change in d_p between cloud base and surface (1-d_{sf}/d_{cb}) for 21 out of the 22 P3 cases where the rain reaches the surface after partial evaporation. Circle color codes are red, blue, green, and black for 4, 5, 9, and 10 February respectively. The black line represents a linear fit of y=0.59x+0.18 with a correlation coefficient (r) of 0.62 and p-value of 0.07. Note that the 4 February cases (red circles) have REF smaller than 1. The x-axis values higher than 1 are for cases where d_{cb} is positive but d_{sf} is negative, causing 1-d_{sf}/d_{cb} to be higher than 1.
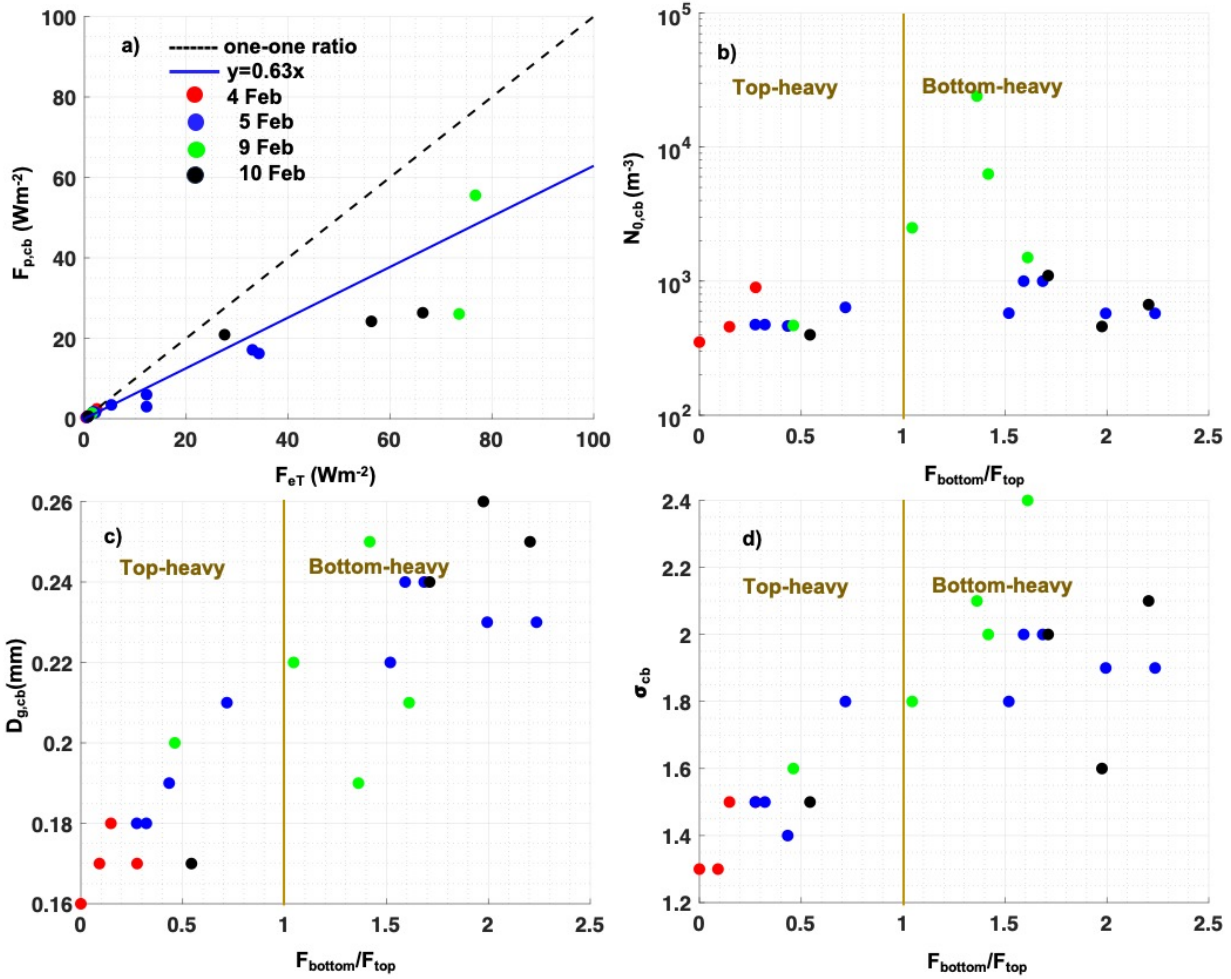
Figure 9. a) Rain flux at cloud base ($F_{p,cb}$) is scattered against column total sub-cloud rain evaporation flux (F_{eT}). Only 20 out of 22 cases are shown, excluding the highest two cases on 9 February with F_{eT} above 300 Wm^{-2}. The 4, 5, 9, and 10 February cases are shown in red, blue, green, and black filled circles, respectively. The blue line is the slope through all 22 cases and is 0.63. The dashed black line is the one-to-one ratio line for reference. The F_{bottom}/F_{top} ratio is plotted with b) $N_{o,cb}$, c) $D_{g,cb}$ and d) σ_{cb}. F_{top} and F_{bottom} are the summation of F_e over 350-700m and 0-350m, respectively. F_{bottom}/F_{top} higher than 1 denotes bottom-heavy and less than 1 denotes top-heavy cases, as mentioned in gold letters.
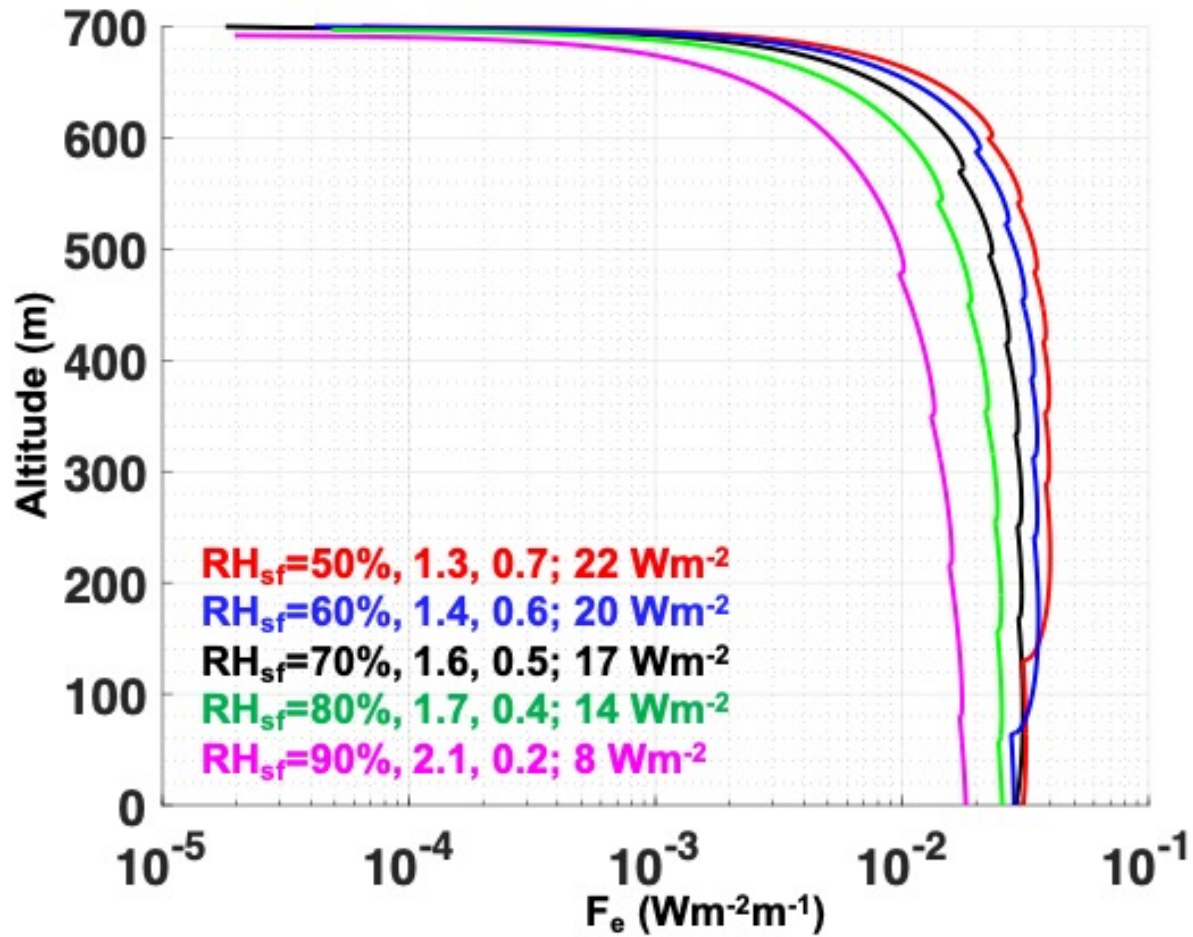
Figure 10. F_e profiles modeled with altitude for RH_{sf} of 50% (red), 60% (blue), 70% (black), 80% (green) and 90% (magenta), respectively. The RH_{sf} is followed by the F_{bottom}/F_{top}, REF and F_{eT} in the legend.
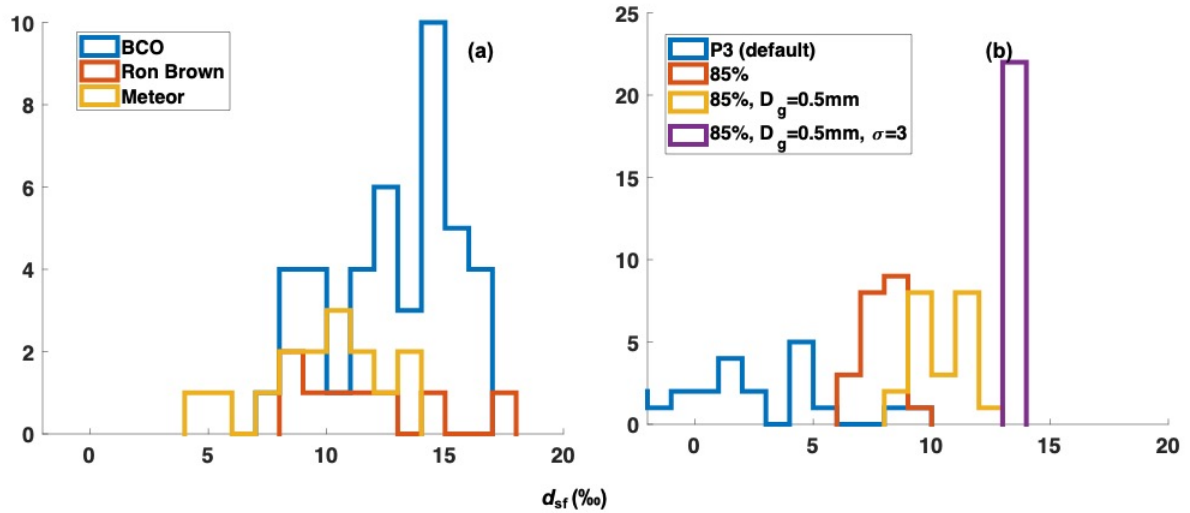
Figure 11. a) Histograms of surface d_p (d_{sf}) observed by the Brown (red), Meteor (yellow), and BCO (blue). b) Histograms of modeled surface d_p for all the P3 cases run at observed cloud base D_g (0.16-0.26 mm), σ (1.2-2.4), d_p (7-15‰) and RH_{sf} (66-87%) (blue, default condition). Histograms of the P3 cases run at default D_g, σ and d_p but at RH_{sf} of 85% (red). Histograms of the P3 cases run at default σ and d_p but at RH_{sf} and D_g of 85% and 0.5 mm, respectively (yellow). Histogram of modeled d_{sf} at cloud base D_g, σ, d_p and RH_{sf} of 0.3 mm, 3, 14‰ and 85%, respectively (purple).